

# The influence of beam focus during laser powder bed fusion of a high reflectivity aluminium alloy - AlSi10Mg

Sagar Patel<sup>a</sup>, Haoxiu Chen<sup>b</sup>, Mihaela Vlasea<sup>a,\*</sup>, Yu Zou<sup>b</sup>

<sup>a</sup>University of Waterloo, Department of Mechanical and Mechatronics Engineering, Waterloo, ON N2L 3G1, Canada

<sup>b</sup>University of Toronto, Department of Materials Science and Engineering, Toronto, ON M5S3E4, Canada

---

## Abstract

The laser powder bed fusion (LPBF) of aluminium alloys is associated with numerous challenges when compared to other commonly used alloys (e.g., steels and titanium alloys) due to their higher reflectivity and thermal conductivity. This leads to a higher defect density in the final parts, commonly related to melt pool instabilities in the transition and keyhole melting modes. In this work, processing diagrams, temperature prediction models, X-ray computed tomography (XCT), and metallography are used for establishing criteria in process parameter optimization of high reflectivity aluminium alloys based on AlSi10Mg response in using 57 different power, velocity, and beam diameter combinations. For LPBF systems with focused beam diameters  $<100\text{ }\mu\text{m}$ , divergent beams obtained by defocusing to a position above the LPBF build plate primarily lead to conduction mode melt pools, avoiding keyhole mode defects, and resulting in parts with densities  $>99.98\%$ , with effectively no porous defects in the subsurface regions. Additionally, an analytical model guided selection of laser power and velocity settings for a focused beam help in stabilizing melt pool and spatter dynamics in the transition melting mode thereby enabling a potential to obtain density values close to conduction mode densities ( $\sim 99.98\%$ ). A dimensionless keyhole number (Ke) was used in this work to identify distinct regions of conduction (Ke of 0-12), transition (Ke of 12-20), and keyhole (Ke  $> 20$ ) mode melting during LPBF of AlSi10Mg. Lastly, a melt pool aspect ratio (ratio of melt pool depth to width) of  $\sim 0.4$  is observed to be the threshold between conduction and transition/keyhole mode melt pools for AlSi10Mg, different from the conventionally assumed 0.5. This work demonstrates a dimensionless-process map method to obtain near fully dense parts that can be generalised for LPBF of high reflectivity alloys.

**Keywords:** Additive manufacturing, Laser powder bed fusion, Dimensionless process maps, Aluminium alloys, Porosity, AlSi10Mg

---

\*

Email address: [mihaela.vlasea@uwaterloo.ca](mailto:mihaela.vlasea@uwaterloo.ca) (Mihaela Vlasea )

## 1. Introduction

The potential of powder bed fusion (PBF) technologies to produce high-quality complex geometries and the ability to pursue assembly consolidation have been shown to increase technology adoption in the aviation [1, 2, 3, 4, 5, 6, 7] and automotive industries [8, 9, 10, 11, 12] in particular. Laser powder bed fusion (LPBF) is a PBF technology with a high industrial uptake, owing to the minimum feature size resolution and surface finish possible with the reduced beam spot sizes commonly used [13]. The use of smaller achievable beam spot sizes, combined with the advances in design for additive manufacturing (DfAM) competencies, have helped in realizing the true potential of LPBF for light weighting and design optimization of critical components.

Aluminium alloys are commonly used in aerospace and automotive applications, when a combination of high strength performance and low weight is required. As such, AlSi10Mg has been adopted widely in the LPBF community for these applications [14, 15, 16]. The smaller beam spot sizes used in LPBF, however, lead to the lowering of the vaporization threshold of aluminium [17], which can be a disadvantage due to the ease of porosity formation in the keyhole melting mode of aluminium alloys [18]. It has hence been previously assumed in literature that keyhole mode melting is the dominant melting mechanism in LPBF of aluminium alloys such as AlSi10Mg, while working with a beam spot radius of 10  $\mu\text{m}$  [19]. Similarly, for another experimentally intensive effort on processing AlSi10Mg with a beam spot radius of 35  $\mu\text{m}$ , keyhole mode porosity defects were observed in three-dimensional coupons at laser power settings ranging from 88 to 390 W, and scan speeds ranging from 250 mm/s to 2500 mm/s [20]. Based on the literature, there are challenges in identifying stable process parameter windows for obtaining defect-free components for AlSi10Mg due to the rapid onset of keyhole melting mode driven by the interaction of a highly focused energy source acting on a high reflectivity and high thermal conductivity material system [21, 22, 23]. The same can be said in terms of challenges in addressing porous defects in other aluminium alloys, such as A357 [24], AlSi7Mg [25], Scalmalloy [26], Zr-modified Al6061 [27], and Zr-modified Al5083 [28]. Simulations [29] and experiments [30] to understand laser absorptivity during LPBF of aluminium have also pointed towards the significant differences in laser material interaction characteristics for aluminium alloys when compared to low reflectivity materials. High-speed and high-resolution X-ray imaging during LPBF of two aluminium alloys (AlSi10Mg and Al6061) has shown the formation of keyhole instability driven defects even at shallow melt pool depths due to the increased number of laser beam reflections in the vaporized region of Al melt pools [31]. Additionally, melt pool vaporization has been shown to cause large spatter ejecta during LPBF [32] that is capable of blocking the laser beam leading to lack of fusion defects caused by a sudden drop in melt pool depth. The significant differences in absorptivity characteristics for aluminium alloys in the conduction and transition melting modes when compared to titanium, ferrous, and nickel alloys [30]

also contribute towards the difficulties in obtaining defect-free parts as the rapidly increasing vapour cavity in the melt pool would make it difficult for a pore to escape during solidification. One path towards exploring such defect-free process windows is by exploring the effects of beam defocusing on achieving stable conduction-mode [18, 33, 34], as proposed in the present work. Stable conduction mode recipes also help in exploring faster beam velocities and higher hatch distances leading to productivity enhancement for LPBF [33, 35, 36].

The motivation behind exploring defect-free stable conduction mode melting in AlSi10Mg is reinforced by the body of literature studying the effect of conduction, transition, and keyhole modes on microstructures, porosity and resulting mechanical properties of multiple alloy classes [34, 35, 37, 38, 39, 40]. Qi et al. [34] observe a lower crack density in the keyhole melting mode for Al7050 but a higher and more uniform nano-hardness across the melt pool in conduction melting mode. Higher vaporization of Zn and Mg was observed in the keyhole melting mode for Al7050. Aggarwal et al. [37] observe a higher hardness, higher elongation, and finer cellular grains in stable keyhole mode coupons of 316L stainless steel, when compared to conduction mode coupons. Yang et al. [38] report a wider processing window for Ti-6Al-4V in the conduction melting mode and similar tensile properties for conduction and keyhole melting modes, but report a higher elongation for keyhole melting mode coupons. Using micro-scale simulations, Wang and Zou [39] report a more uniform thermal distribution during multi-track LPBF in the conduction mode when compared to keyhole melting mode, leading to a more uniform microstructure in Ti-6Al-4V. Patel et al. [40] reported reduced effects of adhered partially fused powder particles leading to low side-skin surface roughness for LPBF of Ti-6Al-4V using keyhole melting mode parameters when compared to conduction melting mode parameters. For a top-hat shaped laser beam profile, Tenbrock et al. [35] reported >99.95% density components in both the conduction and keyhole melting modes for 316L stainless steel with a gradual transition between the melting modes. A comparably uniform thermal distribution during multi-track printing leading to a uniform microstructure is hence a common characteristic observed in the stable conduction melting mode; with the potential for a finer microstructure, improved side-skin surface finish, and improved tensile properties for the stable keyhole melting mode. It is therefore important to explore methodologies for generating stable conduction mode and keyhole transition mode melting in aluminium alloys.

In this work, a combination of processing diagrams, temperature prediction models, X-ray computed tomography (XCT), and metallography are used to study the effects of focused and divergent Gaussian laser beams during LPBF of 57 different process parameter combinations (21 using focused beams and 36 using divergent beams) during LPBF of AlSi10Mg. Dimensionless processing diagrams [23, 29] are used to identify distinct regions of conduction, transition, and keyhole melting modes during LPBF of AlSi10Mg. A temperature prediction model from previous work [23] is adapted for Al alloys with

the goals of inferring the changes in laser absorptivity in the three melting modes. Additionally, an analytical model for predicting spatter dynamics is used for understanding and predicting high-density process parameter combinations using focused beams.

Deploying a process parameter strategy resulting in a drastic reduction in porous defects, specifically in the subsurface regions, would help improve part performance, as porous defects are the most likely site for crack initiation [41, 42, 43, 44, 45]; an example of a subsurface pore (diameter of  $\sim 0.2$  mm) leading to the fatigue crack in AlSi10Mg is shown by Plessis et al. [46]. The approach presented in this work that uses experiments guided by normalized processing diagrams and temperature prediction models helps ease the process parameter optimization efforts for aluminium alloys with high reflectivity and high thermal conductivity, especially for the goals of reducing porosity. The results from this present work will help demonstrate that stable conduction mode melting can be achieved in high reflectivity and high thermal conductivity aluminium alloys, with a drastic reduction in core and sub-surface pore defects. The opportunity to obtain defect-free parts across melting modes during LPBF of aluminium alloys opens up new avenues in terms of tailoring microstructure for application-specific requirements due to significant differences in microstructure reported in literature across melting modes.

## 2. Materials and Methods

A widely studied aluminium alloy, AlSi10Mg, was deployed using a modulated LPBF system (AM 400, Renishaw, UK) to demonstrate the theoretical concepts in this work. The powder used was plasma atomized pre-alloyed AlSi10Mg (AP&C, Montreal, Canada) with a size distribution of 15-63  $\mu\text{m}$  and a D50 of 28  $\mu\text{m}$ . The experimental efforts in this work consists of 2 phases - melt pool analysis using weld lines and investigation of microstructure and porosity using cubes and cylinders respectively.

### 2.1. Melt pool evaluation

The first phase of this study is geared towards understanding the effects of the conduction, transition, and keyhole melting modes on the melt pool behaviour during LPBF of AlSi10Mg. As such, a total of 57 process parameter combinations were evaluated at varying laser powers (150 - 400 W), effective scanning velocities (250 - 1765 mm/s), beam spot radii (35 - 102  $\mu\text{m}$ ), and powder layer thickness values (30 - 50  $\mu\text{m}$ ) as summarized in Table 1.

For the modulated LPBF system used in the present study (AM 400, Renishaw, UK), the effective laser power,  $P_{eff}$  is obtained from [23] and is given by Equation 1. Similarly, the effective beam velocity,  $v$ , is given by Equation 2. In Equation 1,  $P$  is the actual laser power used in the modulated LPBF system,  $t_e$  is the time when the laser is acting on the material (exposure time,  $\mu\text{s}$ ) and  $t_d$  is the time when the laser is turned off and is re-positioning to the next exposure point (also referred to as the



drill delay time, set as constant 10  $\mu\text{s}$ ). In Equation 2,  $p_d$  is the distance between two consecutive laser exposure points (point distance,  $\mu\text{m}$ ).

$$P_{eff} = \frac{P \cdot t_e}{t_e + t_d} \quad (1)$$

$$v = \frac{p_d}{t_e + t_d} \quad (2)$$

For the modulated LPBF system used in the present study (AM 400, Renishaw, UK), the beam spot radius at the focal point is given by  $r_0 = 35 \mu\text{m}$ , and the wavelength of the laser beam used is  $\lambda = 1070 \text{ nm}$ . To obtain beam radius values  $> 35 \mu\text{m}$  summarized in Table 1, the laser beam was defocused to positions above the build plate, to obtain a divergent beam. The beam radius ( $r_b$ ) values of the defocused beam are then obtained from the equation for a Gaussian distribution of a laser beam given by Equation 3 [47].

$$r_b = r_0 \sqrt{1 + \left( \frac{z\lambda}{\pi r_0^2} \right)^2} \quad (3)$$

For obtaining a beam radius of  $54 \mu\text{m}$  with the Renishaw AM 400, a defocusing distance of  $z = 4.2 \text{ mm}$  was used,  $z = 5.5 \text{ mm}$  was used to obtain a beam radius of  $64 \mu\text{m}$ ,  $z = 6.6 \text{ mm}$  was used to obtain a beam radius of  $73 \mu\text{m}$ ,  $z = 7.8 \text{ mm}$  was used to obtain a beam radius of  $84 \mu\text{m}$ ,  $z = 8.7 \text{ mm}$  was used to obtain a beam radius of  $92 \mu\text{m}$ , and  $z = 9.9 \text{ mm}$  was used to obtain a beam radius of  $102 \mu\text{m}$ .

Table 1: LPBF processing parameters for evaluating the effect of melting modes on melt pool and porosity behaviour in AlSi10Mg. Laser power -  $P$ , point distance -  $p_d$ , exposure time -  $t_e$ , beam radius -  $r_b$ , layer thickness -  $l_t$ , hatch distance -  $h_d$ , effective laser power -  $P_{eff}$ , and effective velocity -  $v$ . The drill delay time,  $t_d$ , is constant for the Renishaw AM 400 at 10  $\mu\text{s}$ .

Sample code	$P$ [W]	$r_b$ [ $\mu\text{m}$ ]	$p_d$ [ $\mu\text{m}$ ]	$t_e$ [ $\mu\text{s}$ ]	$l_t$ [ $\mu\text{m}$ ]	$h_d$ [ $\mu\text{m}$ ]	$P_{eff}$ [W]	$v$ [mm/s]
1	300	54	55	60	30	100	257	786
2	350	54	55	80	30	100	311	611
3	150	35	55	60	30	100	129	786
4	180	35	55	70	30	100	158	688
5	200	35	55	90	30	100	180	550
6	240	35	55	100	30	100	218	500
7	150	54	55	80	30	100	133	611
8	200	54	55	100	30	100	182	500

Continued on next page

Table 1 – Continued from previous page

Sample code	$P$ [W]	$r_b$ [ $\mu\text{m}$ ]	$p_d$ [ $\mu\text{m}$ ]	$t_e$ [ $\mu\text{m}$ ]	$l_t$ [ $\mu\text{m}$ ]	$h_d$ [ $\mu\text{m}$ ]	$P_{eff}$ [W]	$v$ [mm/s]
9	200	54	55	60	30	100	171	786
10	250	54	55	80	30	100	222	611
11	250	54	55	60	30	100	214	786
12	300	54	55	100	30	100	273	500
13	300	54	55	80	30	100	267	611
14	350	54	55	60	30	100	300	786
15	400	54	55	100	30	100	364	500
16	400	54	55	80	30	100	356	611
17	400	54	55	60	30	100	343	786
18	200	64	55	60	30	100	171	786
19	250	64	55	60	30	100	214	786
20	300	64	55	60	30	100	257	786
21	350	64	55	60	30	100	300	786
22	400	64	55	60	30	100	343	786
23	200	74	55	60	30	100	171	786
24	250	74	55	60	30	100	214	786
25	300	74	55	60	30	100	257	786
26	350	74	55	60	30	100	300	786
27	400	74	55	60	30	100	343	786
28	200	84	55	60	30	100	171	786
29	250	84	55	60	30	100	214	786
30	300	84	55	60	30	100	257	786
31	350	84	55	60	30	100	300	786
32	400	84	55	60	30	100	343	786
33	200	93	55	80	30	100	178	611
34	250	93	55	80	30	100	222	611
35	300	93	55	80	30	100	267	611
36	350	93	55	80	30	100	311	611
37	400	93	55	80	30	100	356	611
38	300	102	55	100	30	100	273	500

Continued on next page

Table 1 – Continued from previous page

Sample code	$P$ [W]	$r_b$ [ $\mu\text{m}$ ]	$p_d$ [ $\mu\text{m}$ ]	$t_e$ [ $\mu\text{m}$ ]	$l_t$ [ $\mu\text{m}$ ]	$h_d$ [ $\mu\text{m}$ ]	$P_{eff}$ [W]	$v$ [mm/s]
39	350	102	55	100	30	100	318	500
40	400	102	55	100	30	100	364	500
41	240	35	45	60	50	100	206	643
42	240	35	60	60	50	100	206	857
43	240	35	75	75	50	100	212	882
44	200	35	60	170	50	100	189	333
45	200	35	60	119	50	100	184	465
46	200	35	60	60	50	100	171	857
47	156	35	60	110	35	140	143	500
48	193	35	60	70	35	140	169	750
49	234	35	60	50	35	140	195	1000
50	390	35	60	24	35	140	275	1765
51	212	35	60	110	35	175	194	500
52	270	35	60	70	35	175	236	750
53	334	35	60	50	35	175	278	1000
54	177	35	60	110	35	142	162	500
55	193	35	60	70	35	140	169	750
56	255	35	60	50	35	145	213	1000
57	287	35	60	38	35	132	227	1250

From Table 1, melt pool measurements for sample code labels 7-40 were obtained by printing 5 consecutive weld lines (length 8 mm, using the corresponding process parameters listed) on top of substrate artifacts. The substrate artifacts are cubes of side-length 10 mm which were printed directly on the reduced build volume of the AM 400. The 5 weld lines were separated by a hatch distance of 100  $\mu\text{m}$ . For these samples, meltpool measurements were obtained from the five weld lines, by cross-sectioning the samples perpendicular to the weld lines. The substrate artifacts were manufactured with a laser power of 200 W, point distance of 60  $\mu\text{m}$ , exposure time of 90  $\mu\text{m}$ , and beam spot radius of 54  $\mu\text{m}$ . For the remaining labels, cubes of side-length 10 mm were manufactured using the process parameters given in Table 1, as part a separate print, and a hatch distance of 100  $\mu\text{m}$  to obtain the melt pool depth and half width measurements as shown in Figure 1; such measurements were taken for meltpools where the meltpool depth is fully visible. For these samples, meltpool measurements were

obtained from the top most layer, by cross-sectioning the samples perpendicular to the hatch vector on the top layer. The AlSi10Mg samples were sectioned, polished, and etched with diluted phosphoric acid (9 g phosphoric acid and 100 ml H<sub>2</sub>O) for visualizing the desired meltpools. Micrographs were taken at the top edge of the cubes (VK-X250, Keyence, Japan).

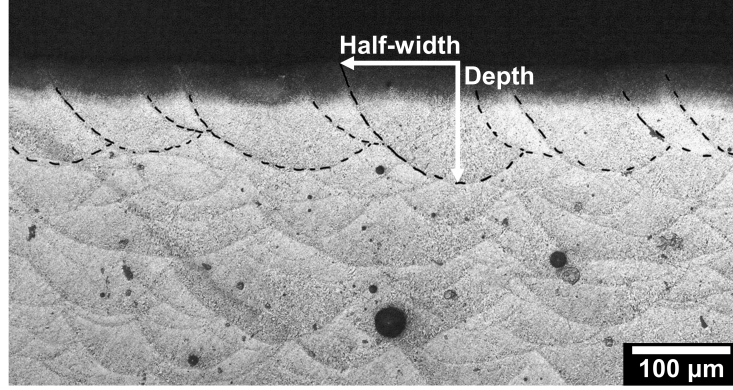


Figure 1: Measurement of the melt pool depth and half-width for one of the melt pools from sample 5.

The melt pool datasets are then analyzed using a normalized processing diagram, based on prior work [23], to evaluate the effect of divergent and focused beams on the melting modes during LPBF of AlSi10Mg using the 57 process parameter combinations from Table 1.  $E^*$  and  $v^*$  in the normalized processing diagrams are given by Equations 4 and 5 respectively.

$$E^* = \frac{AP_{eff}}{2l_t\lambda(T_m - T_0)} \quad (4)$$

$$v^* = \frac{vr_b}{\alpha} \quad (5)$$

In Equation 4,  $E^*$  is the dimensionless heat input,  $A$  is laser absorptivity,  $P_{eff}$  is the effective laser power [W],  $l_t$  is the powder layer thickness [m],  $\lambda$  is the thermal conductivity [W/(mK)],  $T_m$  is the melting temperature [K], and  $T_0$  is the initial (or powder bed) temperature [K] taken as 293 K. In Equation 5,  $v^*$  is the dimensionless beam velocity,  $v$  is the laser beam velocity [m/s],  $r_b$  is the beam radius used [m], and  $\alpha$  is the thermal diffusivity [m<sup>2</sup>/s]. The material properties used for Equations 4 and 5 are taken at the solidus temperature from [48] and are given in Table 2.

The threshold between the conduction and transition/keyhole melting modes during LPBF of AlSi10Mg in the processing diagram used in this work are given by the contour of the dimensionless peak temperature,  $T_p^*$ , based on previous work [23]. The dimensionless peak temperature term,  $T_p^*$ , is given by Equation 6.

Table 2: Thermo-physical properties of AlSi10Mg taken at the solidus temperature [48].

Properties	Material(AlSi10Mg)
Density, $\rho$ [kg/m <sup>3</sup> ]	2670
Thermal conductivity, $\lambda$ [W/(mK)]	113
Specific heat capacity, $C_p$ [J/(kgK)]	565.29
Solidus temperature, $T_s$ [K]	831
Liquidus temperature, $T_m$ [K]	867
Vaporization temperature, $T_v$ [K]	2740
Total latent heat (fusion and vaporization), $H$ [J/kg]	10943000

$$T_p^* = \frac{T_p - T_0}{T_m - T_0} = \frac{3}{2\sqrt{2}\pi e^{0.75}} \cdot \frac{E^*}{v^*} \cdot \frac{1}{(z^* + z_0^*)^2} \quad (6)$$

In Equation 6,  $T_p$  is the peak temperature under consideration, which is considered as the vaporization temperature (boiling point) of a given material,  $T_m$  is the melting point of a given material, and  $T_0$  is the powder bed temperature (which is room temperature for this work, 293 K). The term  $z^*$  is dimensionless depth, obtained as the ratio of the dimension along the depth of a melt pool,  $z$ , and the beam spot radius,  $r_b$ , in Equation 7; this term was first defined by Ion et al. [49]. The term  $z_0^*$  is the dimensionless distance of the apparent heat source above the surface of the melt pool, which is a function of  $v^*$  as given by Equation 8. The detailed derivation for  $T_p^*$  and associated terms is provided in previous work [23].

$$z^* = z/r_b \quad (7)$$

$$z_0^* = \sqrt{\frac{3\sqrt{\pi}}{2\sqrt{2}e^{0.75}} \cdot \frac{1}{v^* \tan^{-1}(\sqrt{8/v^*})}} \quad (8)$$

The threshold between the conduction and transition/keyhole melting modes for AlSi10Mg is given by the temperature contour for the boiling point of aluminium ( $T_p^* = 4.26$ ) at  $z^* = 0$ . The term  $z^* = 0$  corresponds to surface vaporization and the contour in Figure 3 is thereby labeled as the predicted surface vaporization threshold for LPBF of AlSi10Mg, or the threshold between the conduction and transition/keyhole melting modes.

Additionally, to affirm the findings by the normalized processing diagrams, as well as better identify the conduction, transition, and keyhole melting modes during LPBF of AlSi10Mg, a keyhole number ( $Ke$ ) developed by Gan et al. [29] is used in work. The keyhole number parameter,  $Ke$ , is given by Equation 9.

$$Ke = \frac{AP_{eff}}{\pi \rho C_p (T_m - T_0) \sqrt{\alpha v r_b^3}} \quad (9)$$

## 2.2. Microstructure and porosity evaluation

The second phase of this study is geared towards understanding the effects of the conduction, transition, and keyhole melting modes on the microstructure and porosity during LPBF of AlSi10Mg. As such, cubes of side-length 10 mm (for microstructure evaluation) and cylinders of diameter 5 mm and height 9 mm (for porosity evaluation) were printed on the reduced build volume (RBV) of the AM 400 system. Six sets of processing parameters given by parameters sample code labels 1-6 (labels 1 and 2 from conduction mode, labels 3 and 4 from transition mode, and label 5 and 6 from keyhole mode), from Table 1 were investigated. The hatching distance was kept constant at 100  $\mu\text{m}$  for all cubes and cylinders. The scan order was set such that the hatch volume (core) was scanned first, followed by the border; the border scans having the same set of processing parameters as the core. Border scans are commonly used in LPBF to improve the dimensional accuracy and surface roughness of LPBF coupons [50]; surface topography optimization was beyond the scope of this present work. The meander scan strategy was used with a 67° rotation between each layer, to reduce residual stresses, anisotropy, surface roughness and promote lower rates of defect propagation by the virtue of the scan vector direction not repeating for 180 layers [51, 52, 53].

The AlSi10Mg cylinders were analyzed for porosity characteristics by a 3D X-ray computed tomography (XCT) scanner (ZEISS Xradia 520 Versa) using a 6  $\mu\text{m}$  voxel size. To visualize the defect distribution within each sample, the CT scanned files were analyzed using an image processing software (Dragonfly 3.0, Object Research Systems Inc., Montreal, QC). The AlSi10Mg cubes were sectioned, polished, and etched with diluted phosphoric acid (9 g phosphoric acid and 100 ml  $\text{H}_2\text{O}$ ) for studying their microstructure. Micrographs were taken at various locations including the top edge and core of the cubes (VK-X250, Keyence, Japan).

## 3. Results and discussion

In this work, laser beam defocusing was studied, primarily with the intent of understanding how to achieve low porosity parts via stable conduction mode and steady-state transition mode LPBF process parameters for AlSi10Mg. The literature discussed in detail in Section 3.1 indicates that during the

LPBF of AlSi10Mg, conduction mode melting is not reported for beam spot radiuses below 50  $\mu\text{m}$ . Since the Renishaw AM 400 has a beam spot radius of 35  $\mu\text{m}$  at the focal plane, a transition or keyhole melting mode is hence expected, unless the beam is defocused. The defocusing of the beam was kept to positions above the build plate to create a divergent beam effect at the laser-material interaction plane, instead of a convergent beam effect obtained by defocusing to positions below the build plate.

### 3.1. Melt pool evaluation based on melting modes

The effect of the divergent beam defocusing strategy is illustrated in Figure 2, wherein numerous large keyhole-type defects are generally observed for the samples built with the focused beam approach (for this study, a beam spot radius of 35  $\mu\text{m}$ ), whereas a conduction mode type microstructure with a few minor defects are observed for the samples built with the divergent beam. Such minor defects captured in conduction mode melting of AlSi10Mg can be attributed to hydrogen-induced defects in aluminium alloys as reported by Weingarten et al. [54]. The melt pool outcomes, including the melt pool depths, width, and aspect ratios (melt pool depth/width) along with the values of dimensionless parameters used in this section are given in Table 3.

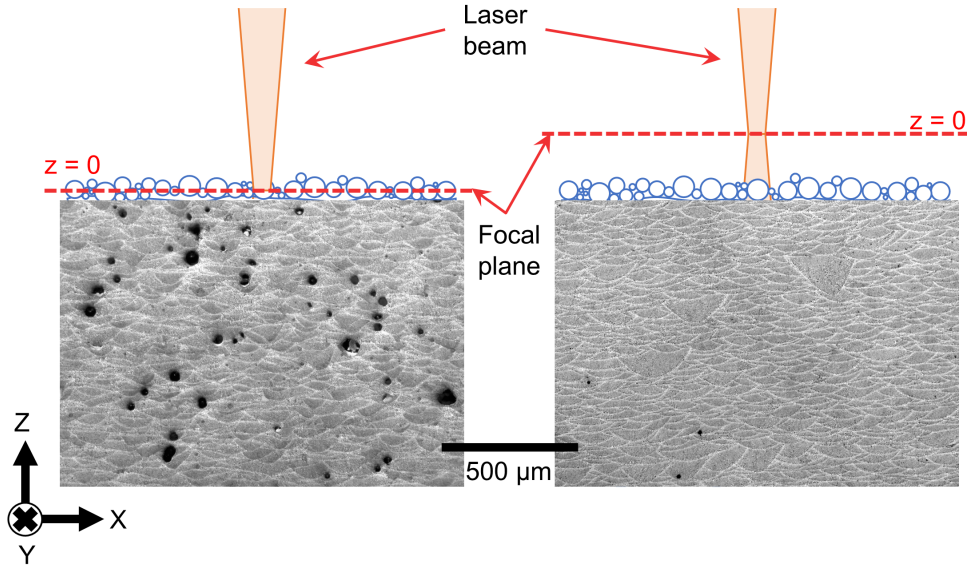


Figure 2: Typical microstructure of AlSi10Mg obtained with the focused beam (left, sample 5) and with the defocused beam (right, sample 2). The focused laser beam microstructure consists of numerous defects related to excessive vaporization in the keyhole mode, while a few hydrogen solubility related defects are observed by using a diverging defocused beam.

The normalized processing diagram illustrated in Figure 3 is used to evaluate the effect of divergent and focused beams on the melting modes during LPBF of AlSi10Mg using the 57 process parameter combinations from Table 1. The absorptivity values used in the  $E^*$  term (Equation 4) and given by

the inferred absorptivity columns in Table 3 were obtained inversely by comparing the predicted melt pool depths with experimental measurements (also given in Table 3). The average measured melt pool depth was used to inversely calculate the average inferred absorptivity, while the highest and lowest values within the confidence interval of the melt pool depth were used to calculate the variation in inferred absorptivity. The melt pool depth is substituted in the equation for  $z^*$  (Equation 7), and by setting a value of  $T_p^* = 1$ , the absorptivity is calculated through the  $E^*$  term in Equation 6. The calculation for absorptivity using this method now becomes a numerical problem, for which MATLAB's built-in 'vpasolve' function is deployed. The values for the error bars for  $E^*$  in Figure 3 are calculated by substituting the variation in inferred absorptivity into the  $A$  term in Equation 4.

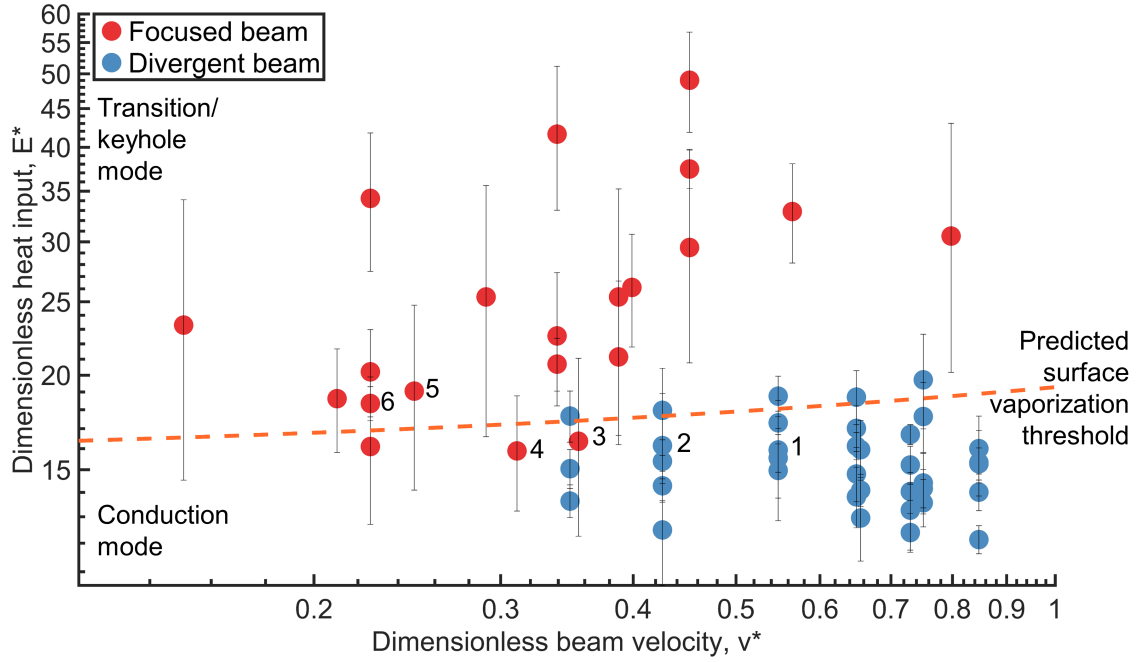


Figure 3: Normalized processing diagram for the 57 AlSi10Mg process parameters used in this study grouped by the use of focused and divergent beams. Samples codes 1-6 used for defect space evaluation in sections 3.2 and 3.3 are labelled in the figure.



Table 3: Melt pool outcomes (depth, width, and aspect ratios) and dimensionless parameters for the 57 process parameter combinations from Table 1. Dimensionless heat input -  $E^*$ , dimensionless beam velocity -  $v^*$ , inferred laser absorptivity -  $A$ , keyhole number -  $Ke$ .

Sample code	$E^*$	$v^*$	$A$	$Ke$	Melt pool		Melt pool		Aspect ratio
					depth ( $\mu\text{m}$ )		width ( $\mu\text{m}$ )		
					Avg.	Std. dev.	Avg.	Std. dev.	
1	15.93	0.55	0.24	7.61	68.25	4.69	199.65	3.46	0.34
2	16.14	0.43	0.2	8.75	79.35	3.26	213.1	23.83	0.37
3	16.36	0.36	0.5	14.98	57.51	15.45	143.01	12.77	0.4
4	15.89	0.31	0.39	15.55	59.98	10.58	136.05	17.05	0.44
5	19.05	0.25	0.41	20.85	80.44	20.71	187.49	58.54	0.43
6	18.35	0.23	0.33	21.06	81.67	3.95	170	35.14	0.48
7	12.49	0.43	0.36	6.77	59.99	11.44	175.48	35.44	0.34
8	13.64	0.35	0.29	8.17	74.04	4.08	205.47	25.63	0.36
9	14.97	0.55	0.34	7.15	63.93	5.61	179.99	13.24	0.36
10	14.29	0.43	0.25	7.74	69.83	3.37	201.64	7.92	0.35
11	15.55	0.55	0.28	7.43	66.57	12.68	214.04	15.88	0.31
12	15.05	0.35	0.21	9.01	82.3	5.06	223.11	13.74	0.37
13	15.39	0.43	0.22	8.34	75.57	5.19	218.15	12.86	0.35
14	17.3	0.55	0.22	8.27	74.19	2.62	204.36	15.77	0.36
15	17.66	0.35	0.19	10.58	96.59	7.23	251.37	23.96	0.38
16	17.97	0.43	0.2	9.74	88.21	11.22	256.91	38.46	0.34
17	18.76	0.55	0.21	8.96	80.27	4.71	219.89	16.46	0.37
18	13.82	0.65	0.31	5.12	63.1	6.58	213.2	17.61	0.3
19	14.81	0.65	0.27	5.48	68.14	6.09	206.03	17.97	0.33
20	16.12	0.65	0.24	5.97	74.56	3.18	215.94	6.6	0.35
21	17.01	0.65	0.22	6.3	78.78	5.52	228.52	19.66	0.34
22	18.71	0.65	0.21	6.93	86.49	6.81	246.73	5.4	0.35
23	13.57	0.75	0.31	4.04	65.8	5.48	204.39	5.45	0.32
24	14.17	0.75	0.26	4.22	69.16	4.53	213.35	7.86	0.32
25	14.41	0.75	0.22	4.29	70.46	7.23	208.72	21.1	0.34
26	17.64	0.75	0.23	5.25	87.14	9.24	254.41	22.05	0.34
Continued on next page									

Table 3 – Continued from previous page

Sample code	$E^*$	$v^*$	$A$	$Ke$	Melt pool		Melt pool		Aspect ratio
					depth ( $\mu\text{m}$ )		width ( $\mu\text{m}$ )		
					Avg.	Std. dev.	Avg.	Std. dev.	
27	19.72	0.75	0.22	5.87	97.1	13.18	262.19	17.52	0.37
28	12.13	0.85	0.28	3.01	60.47	3.26	206.97	22.57	0.29
29	14.01	0.85	0.25	3.48	71.9	4.59	247.67	20.52	0.29
30	15.34	0.85	0.23	3.81	79.5	8.55	267.62	12.59	0.3
31	15.28	0.85	0.2	3.8	79.15	4.18	253.42	12.78	0.31
32	16	0.85	0.18	3.97	83.15	8.9	249.12	21.4	0.33
33	12.39	0.73	0.27	2.99	75.05	5.44	245.24	6.39	0.31
34	13.27	0.73	0.23	3.21	81.43	11.24	238.8	17.81	0.34
35	14.04	0.73	0.2	3.39	86.9	2.58	283.12	9.64	0.31
36	15.22	0.73	0.19	3.68	95	5.94	297.45	24.59	0.32
37	16.7	0.73	0.18	4.04	104.72	3.23	319.7	8.21	0.33
38	12.95	0.66	0.18	3.01	92.41	13.85	322.46	22.89	0.29
39	14.1	0.66	0.17	3.28	101.83	5.61	323.66	21.43	0.31
40	15.95	0.66	0.17	3.71	116.31	10.97	354.77	7.05	0.33
41	25.37	0.29	0.8	42.8	112.6	26.73	263.2	49.39	0.43
42	25.37	0.39	0.8	37.07	112	20.58	245.2	34.72	0.46
43	26.12	0.4	0.8	37.61	112.4	9.61	254.8	29.75	0.44
44	23.29	0.15	0.8	54.56	124.6	44.22	244.8	72.84	0.51
45	18.62	0.21	0.65	36.94	86	12.51	184	26.46	0.47
46	21.14	0.39	0.8	30.89	82	14.09	195.6	19.36	0.42
47	16.1	0.23	0.51	21.56	72	15.95	157.6	23.34	0.46
48	22.54	0.34	0.61	24.64	79.4	13.94	178	29.9	0.45
49	29.49	0.45	0.69	27.92	85.4	22.01	190.4	30.05	0.45
50	30.53	0.8	0.5	21.76	65	19.61	141.2	22.39	0.46
51	34.24	0.23	0.8	45.85	141.8	21.42	278.8	8.07	0.51
52	41.63	0.34	0.8	45.51	133.4	19.98	238	23.79	0.56
53	49.04	0.45	0.8	46.44	128.2	13.18	256.8	18.9	0.5
54	20.21	0.23	0.57	27.06	89.2	10.62	189.6	20.76	0.47

Continued on next page

Table 3 – Continued from previous page

Sample code	$E^*$	$v^*$	$A$	$Ke$	Melt pool		Melt pool		Aspect ratio
					depth (μm)		width (μm)		
					Avg.	Std. dev.	Avg.	Std. dev.	
55	20.68	0.34	0.56	22.61	73.6	5.32	175.6	10.99	0.42
56	37.44	0.45	0.8	35.45	110	4.3	205.2	20.08	0.54
57	32.9	0.57	0.66	27.86	82.8	9.73	158.4	12.12	0.52

An overwhelming majority of the sample codes using divergent beams are observed to lie beneath the predicted surface vaporization threshold (conduction mode), while the samples codes using a focused beam are generally observed to lie above the surface vaporization threshold (transition and keyhole modes), as illustrated in Figure 3. The defocusing strategy is particularly relevant for LPBF systems with smaller beam spot radii (10-35  $\mu\text{m}$ ) [19, 20], wherein transition and keyhole mode melt pools have been reported for all ranges of powers of 100 – 400 W for AlSi10Mg. For AlSi10Mg melt pool datasets reported with systems such as EOS M290 with a higher beam spot radius of 50  $\mu\text{m}$  at the focal point, most melt pools reported were observed to lie in the conduction melting mode, except for power settings above 275 W [55, 56]. Divergent beams help in reducing the onset of keyhole and keyhole pores by reducing the effective beam power density as the melt pool formation progresses and have been used successfully in the laser welding of aluminum alloys [18] and LPBF of 316L stainless steel [33]. When a divergent beam is used, a keyhole depression (if any) during LPBF moves away from the focal plane, leading to a decrease in power density as the melt pool formation progresses into the previously solidified metal. Thus, a divergent beam restricts a potential keyhole cavity from any further growth. On the other hand, a convergent beam exposes the keyhole cavity to an increasing powder density as melt pool formation progresses. Thus, even a shallow keyhole cavity is enough to grow into a deep keyhole and subsequently produce a large melt pool when a convergent beam is used, as shown by Pastor et al. [18] for laser welding, and Metelkova et al. for LPBF [33]. The cause of the observed absence of keyhole pores using divergent beams could be associated to a deviance of the beam profile from a Gaussian distribution to resemble more closely a top-hat distribution during the divergence of the beam as shown by Nie et al. [57]. Assuming this deviance of the beam profile, the threshold power required for surface vaporization (commonly assumed to be the threshold between the conduction and transition modes) would be higher for divergent beams when compared to focused beams, when all other variables are kept constant. This statement is also supported by the temperature prediction models proposed by Graf et al. [58] for predicting the threshold of surface vaporization for Gaussian

and top-hat beam profiles for materials with high thermal conductivity and low surface tension such as aluminium and copper alloys. Graf et al. [58] show that in a Gaussian beam, when all other variables are held constant, a lower power is needed for initiating surface vaporization due to the higher peak intensity in Gaussian beam profiles, when compared to the top-hat distribution. For LPBF systems with beam spot radii  $< 50 \mu\text{m}$ , such as the Renishaw AM 400 used in this work, divergent laser beams are hence required to reduce the effect energy density and achieve conduction mode melt pools.

The temperature prediction model used for Figure 3 has some limitations such as assumptions of a 2D heat source, temperature independent material properties, oversimplification of powder layer thickness effects, and ignorance of heat loss by refraction in the vapour plume [23], which would contribute to the uncertainty margins in the identified surface vaporization threshold. In addition, the latent heat of fusion, thermo-capillary phenomena (Marangoni effect), recoil pressure, and varying laser power absorptivity due to its angle of incidence (Brewster effect) are not incorporated into this modelling approach which could add to uncertainties [59, 60]. Additionally, 9 out of the 21 of the transition and keyhole mode melt pools had inferred absorptivity values  $> 0.8$ , which are higher than experimentally measured limits of absorptivity during LPBF [30, 61, 62]. This is mainly due to the model limitations of not accounting for the effects of recoil pressure on the melt pool depth, which is particularly significant after the onset of surface vaporization in the transition and keyhole melting modes [63]. For these 9 sets of process parameters, an average absorptivity value of 0.8 was assumed. The use of standard deviation bars for  $E^*$  as inferred inversely via the melt pool datasets are also a reflection of some of the limitations in experimentally validating the precise location of each experimental point in the process map. Despite the assumptions and limitations of the present model, such dimensionless process maps are of utility in experimental planning and in explaining experimental outcomes based on laser-material interaction phenomena.

Recent attempts by Gan et al. [29] to develop universal scaling laws for keyhole porosity in LPBF make use of exponential absorptivity scaling laws for titanium, ferrous, and aluminium alloys. The absorptivity law used by Gan et al. [29] was derived by Ye et al. [62] using in-situ micro-calorimetry measurements of absorptivity during LPBF of low reflectivity titanium, ferrous, and nickel alloys. While Gan et al. [29] use simulations to derive the same scaling law for high reflectivity aluminium alloys as well, the recommendations by Gan et al. [29] do not hold true for aluminium alloys when applied to the experimental melt pool datasets in this work, as well as previous work [20]. The inferred absorptivity calculations from melt pool data, as proposed in this work follow the experimentally measured values of absorptivity by Trapp et al. [30] much more closely. Further work is needed on deriving absorptivity scaling laws for high reflectivity aluminium and copper alloys, as the first attempt at in situ absorptivity measurements during LPBF of copper also suggest a significant difference when compared to low reflectivity materials [64].

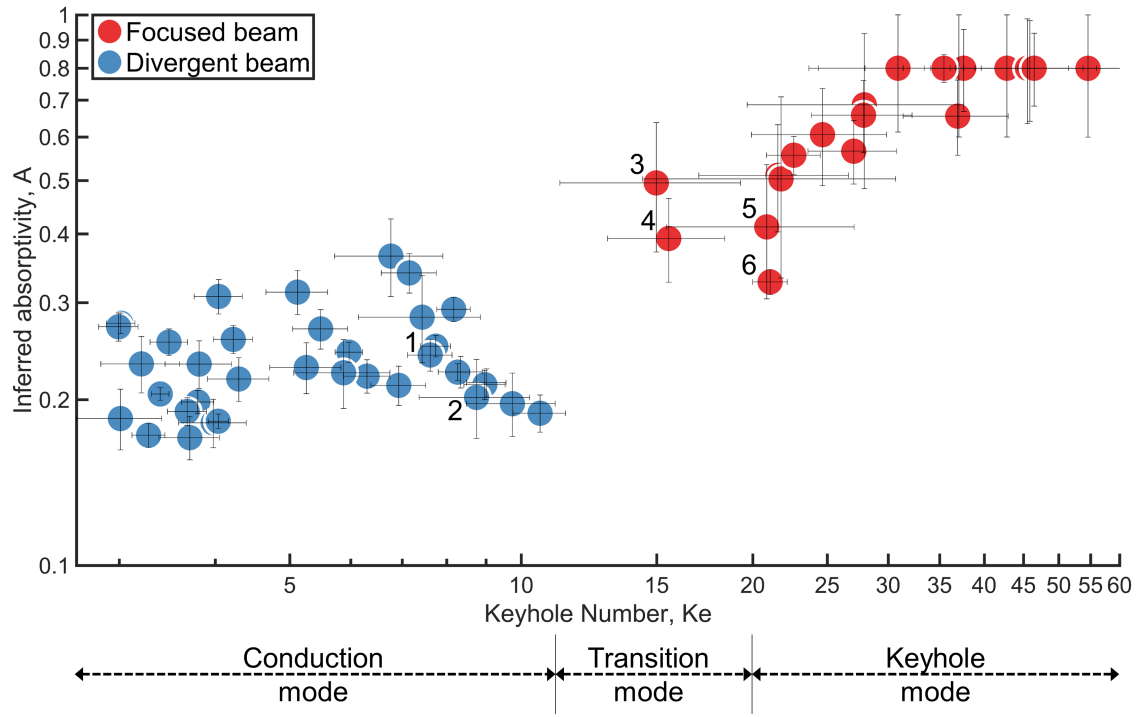


Figure 4: Keyhole number versus inferred absorptivity plot for the 57 AlSi10Mg process parameters used in this study grouped by the use of focused and divergent beams. Samples codes 1-6 used for defect space evaluation in sections 3.2 and 3.3 are labelled in the figure.

To offset the limitations of using the normalized processing diagram resulting in uncertainty in identifying melting mode thresholds, and thus to better identify the conduction, transition, and keyhole melting modes, a keyhole number ( $Ke$ ) developed by Gan et al. [29] is plotted versus the inferred absorptivity values in Figure 4. As depicted in Figure 4, the onset of surface vaporization brings about a more pronounced change in laser absorption and thereby in melt pool behaviour for high reflectivity materials such as aluminium alloys. This is because the onset of surface vaporization adds to additional absorptivity ( $A$ ) of the laser beam in the material that is equal to  $1 - R^N$ , where  $R$  is the reflectivity of a material, and  $N$  is the number of reflections occurring in the vaporized cavity of the melt pool [58]. Materials such as aluminium alloys with higher reflectivity values compared to titanium, ferrous, and nickel alloys would thereby be expected to have differences in melt pool behaviour (melt pool dynamics and thereby solidified melt pool geometry) after the onset of surface of vaporization is crossed. This points towards the differences in absorptivity values that were obtained for the conduction mode points using divergent beams and transition and keyhole mode points using focused beams.

Table 3 shows that conduction mode melt pools (based on Figure 3) obtained using divergent beams have aspect ratios (melt pool depth/width) of  $0.33 \pm 0.03$ , whereas the transition and keyhole mode melt pools obtained using focused beams have aspect ratios of  $0.47 \pm 0.04$ . By these melt pool aspect ratios, based on existing literature [23, 65, 66, 67, 35], it would mean that all the 57 process parameter combination would be expected to lie in the conduction melting mode; however, the optical micrographs of the numerous samples along the build direction (Z-axis) in Figures 5 and 8 shows otherwise. Optical micrographs from most of the process parameter combination that use focused beams shown in Figures 5 and 8 reveal numerous rounded defects representative of keyhole instabilities implying that these sets of processing parameters likely lie in the keyhole melting mode. Hence, a melt pool aspect ratio of 0.4 is more representative of the threshold between the conduction and keyhole melting modes during LPBF of AlSi10Mg; this finding further refines on the 0.5 aspect ratio threshold in literature [23, 65, 66, 68]. Keyhole numbers of 0-12 in Figure 4 are predicted to lie in the conduction melting mode (melt pool aspect ratios  $< 0.4$ ). Samples 3 and 4 have keyhole numbers of 12-20 that are predicted to lie in the transition melting mode based on the analysis provided in section 3.2 and 3.3; this range of 12-20 also matches the regime of "stable keyholes" using ultrahigh-speed synchrotron X-ray imaging during LPBF of Ti-6Al-4V, Al6061, and SS316L in work by Gan et al. [29]. Keyhole numbers  $> 20$  are predicted to lie the keyhole melting mode during LPBF of AlSi10Mg; keyhole numbers  $> 20$  also correspond to the "chaotic keyholes" regime in the work by Gan et al. [29]. The absorptivities value obtained for conduction mode melt pools using divergent beams is  $0.24 \pm 0.05$ , whereas absorptivity values of  $0.65 \pm 0.16$  are obtained using a focused beam for the transition and keyhole mode melt pools respectively.

### 3.2. Porous defect outcomes across melting modes based on micrographs

The effect of the three melting modes (conduction, transition, and keyhole) on melt pool morphologies and porosity was studied using optical micrographs of two conduction mode samples (1 and 2), two transition mode samples (3 and 4), and two keyhole mode samples (5 and 6) along the build direction (Z-axis). Representative illustrations of results are provided in Figure 5. The transition mode samples (3 and 4) seem to have a similar porosity level to the conduction mode samples (1 and 2) in the microstructural images shown in Figure 5, but there are qualitative differences between the melt pool morphologies. The qualitative differences between the melt pool morphologies of samples 3 and 4 (transition mode) with respect to samples 1 and 2 (conduction mode) are apparent by virtue of more variability in the melt pool layer-by-layer organization. The quantitative differences between the melt pool morphologies of samples 1 and 2 are better represented in Table 3 by the lower standard deviations of their melt pool depths when compared to samples 3, 4, and 5. Additionally, samples 3 and 4 seem to have melt pool depths comparable to sample 1 and 2 even when the laser power settings used for them were close to half, which would imply much lower heat inputs. This is due to the onset of vaporization in these samples due to the focused beam, as predicted in the normalized processing diagram in Figure 3.

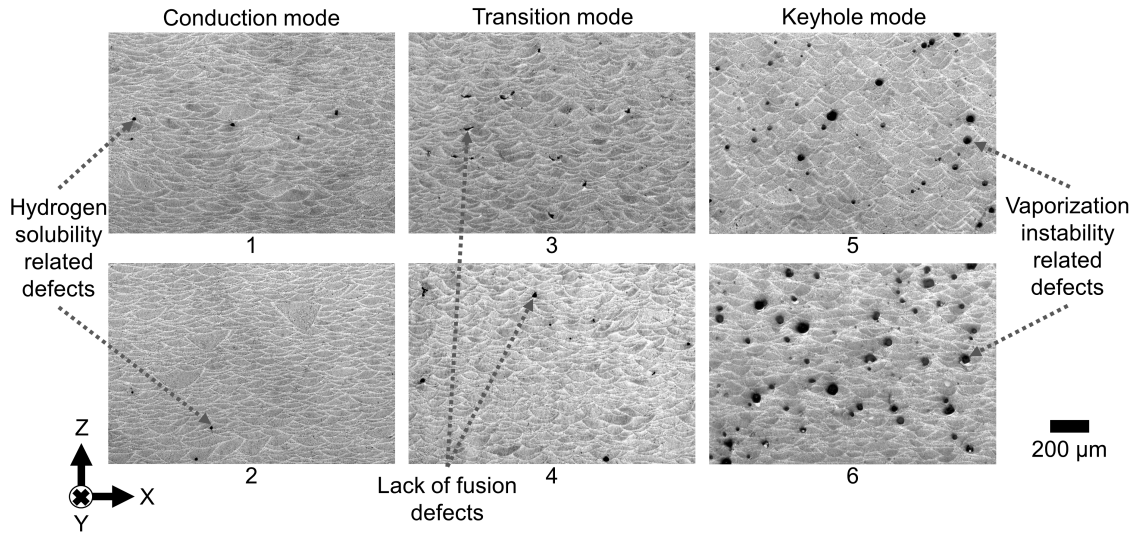


Figure 5: Optical micrographs of the the conduction mode samples (1 and 2), transition mode samples (3 and 4), and keyhole mode samples (5 and 6) along the build direction (Z-axis). Red arrows for sample 4 point to rounded porous defects with diameters of  $\sim 25 \mu\text{m}$ .

In terms of porous defects, samples 1 and 2 (conduction mode) have a small population of defects as shown in Figure 5, with the smallest defects being rounded and commonly attributed to hydrogen-induced defects observed in conduction LPBF of AlSi10Mg; this is also observed by Weingarten et al. [54]. The presence of moisture on the powder surfaces, is one of the main causes attributed to the

reduction of hydrogen solubility in aluminium alloys during the resolidification of liquid aluminium [69]. For samples 5 and 6 (keyhole mode), additional larger defects were observed as seen in Figure 5, particularly at the bottom of melt pool, close to the melt pool boundaries. The source of these defects is expected to be the excessive vaporization of metal expected in keyhole mode melt pools [23]. In conduction mode LPBF of aluminium, where significant vaporization is not expected, the measured absorptivity values for LPBF were  $\sim 0.15$  for a beam spot diameter of  $60 \pm 5 \mu\text{m}$  [30, 61]. However, the high reflectivity in such materials would be expected to aid the overall absorptance significantly once vaporization initiates due to increased number of reflections of the laser beam inside the vaporized region, as observed for aluminium discs in transition mode [30]. High-speed and high-resolution X-ray imaging of two aluminium alloys (AlSi10Mg and Al6061) during LPBF has shown that fluctuations in their vaporized areas of melt pools lead to instabilities and thereby to the formation of porous defects, even with a shallow depth of the vaporization regions in keyhole mode melting due to an increased number of laser beam reflections in the melt pool [31, 29]. Defect generating instances within such melt pools with vaporized regions have also been proven to correspond with a reduced laser absorption at the instance using real time laser absorption measurements alongside melt pool geometry visualization using high-speed synchrotron x-ray imaging by Simonds et al. [70]. A few of the excessive vaporization-related defects are also observed in sample 4 (transition mode), as pointed by the white arrows in Figure 5. Overall, the micrographs support most of the simulation predictions in the normalized process diagram (Figure 3) and keyhole number plot (Figure 4) of samples 1 and 2 being in the conduction mode and samples 5 and 6 being in the keyhole mode. Section 3.3 describes another simulation approach and additional results from X-ray computed tomography to confirm that samples 3 and 4 lie in the transition melting mode. Dimensionless processing diagrams used in the present work are thereby useful tools for reducing the need for iterative design of experiments as they can help with process parameter planning as well as interpreting the physical origin of porous defects during LPBF.

### 3.3. Porous defect outcomes across melting modes based on XCT

To further understand the effects of conduction, transition, and keyhole melting modes on defect formation during LPBF of AlSi10Mg, a visualization of the three-dimensional porous defect space (obtained by XCT) for all six samples are shown in Figure 6. Segmented defects with sizes below 5 interconnected voxels (voxel edge dimension is  $6 \mu\text{m}$ ) have been truncated out from the defect visualization and defect aspect ratio assessments since it is not possible to accurately separate features below this size due to uncertainty in pore segmentation thresholding and instrument noise. The porous defect aspect ratio parameter is the ratio between the minimum and the maximum Feret diameter, where the minimum Feret diameter is the shortest length of a given feature, while the maximum Feret diameter is the longest span of a given feature, as described in [71, 72]. Defects with aspect ratios



above 0.7 were considered as rounded defects in Figures 6 and 7. For calculating the density values shown in Figure 6, all the defects (defects with a voxel size of 1 or more) was considered. The density values are approximations of the true density and a relative assessment of part quality due to the voxel size detection limit. To visualize the locations of the defects, an orthographic projection along the build plate (XY) plane of all the porous defect space for each sample is shown in Figure 7.

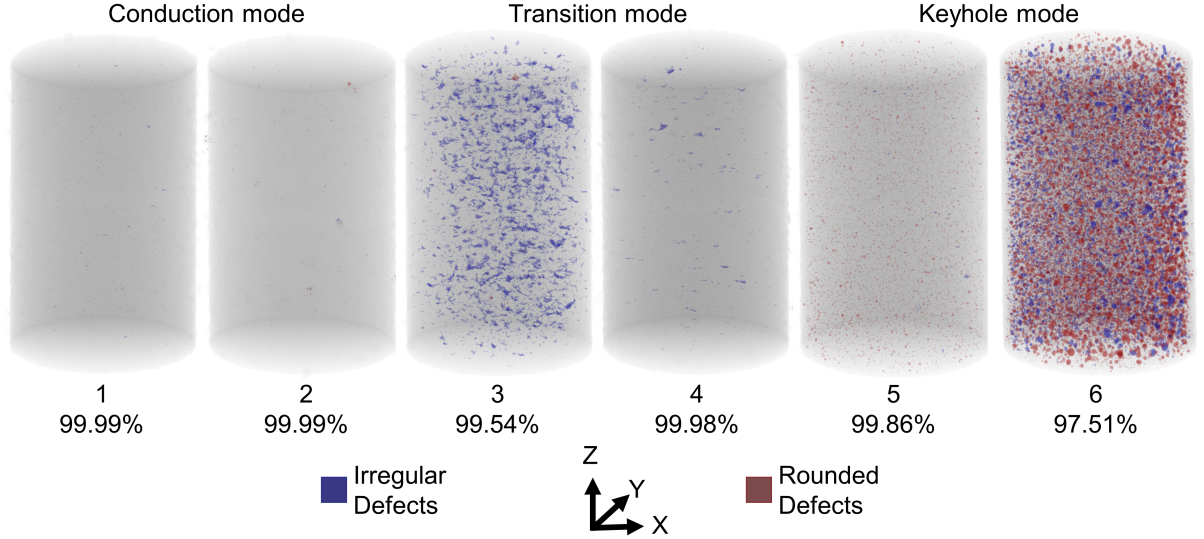


Figure 6: A three-dimensional visualization of the porous defect (above 4 voxels) space along the build direction (Z-axis) from the XCT data of the conduction mode samples (1 and 2), transition mode samples (3 and 4), and keyhole mode samples (5 and 6), along with the density values obtained based on the XCT data. Defects with aspect ratios above 0.7 were considered as rounded defects.

In Figures 6 and 7, it can be observed that sample 1 (conduction mode) has few irregular defects; these are lack of fusion defects, which are attributed to the slightly lower melt pool depths (when compared to sample 2, conduction mode) as noted in Table 2 [73]. There are numerous causes for lack of fusion defects in conduction mode LPBF such as, but not limited to incomplete melting of powder particles within one-layer, incomplete re-melting of material ejecta from previous layers or from neighbouring scan tracks, or incomplete re-melting of irregular surface topographies from previous layers. Such defects can propagate across subsequent layers, resulting in irregularly shaped lack-of-fusion defects [66] that can be observed in Figures 6 and 7.

The defect population in Samples 3 and 4 (transition mode) spans both irregularly shaped and rounded (near spherical) defects as seen in Figures 6 and 7, with a dominance of irregularly shaped defects. While both samples 3 and 4 (transition mode) have similar melt pool dimensions as observed in Table 3, there is a significant difference in the density and frequency of irregularly shaped defects as visible in Figures 6. The main cause for the lower density of sample 3 when compared to sample 4

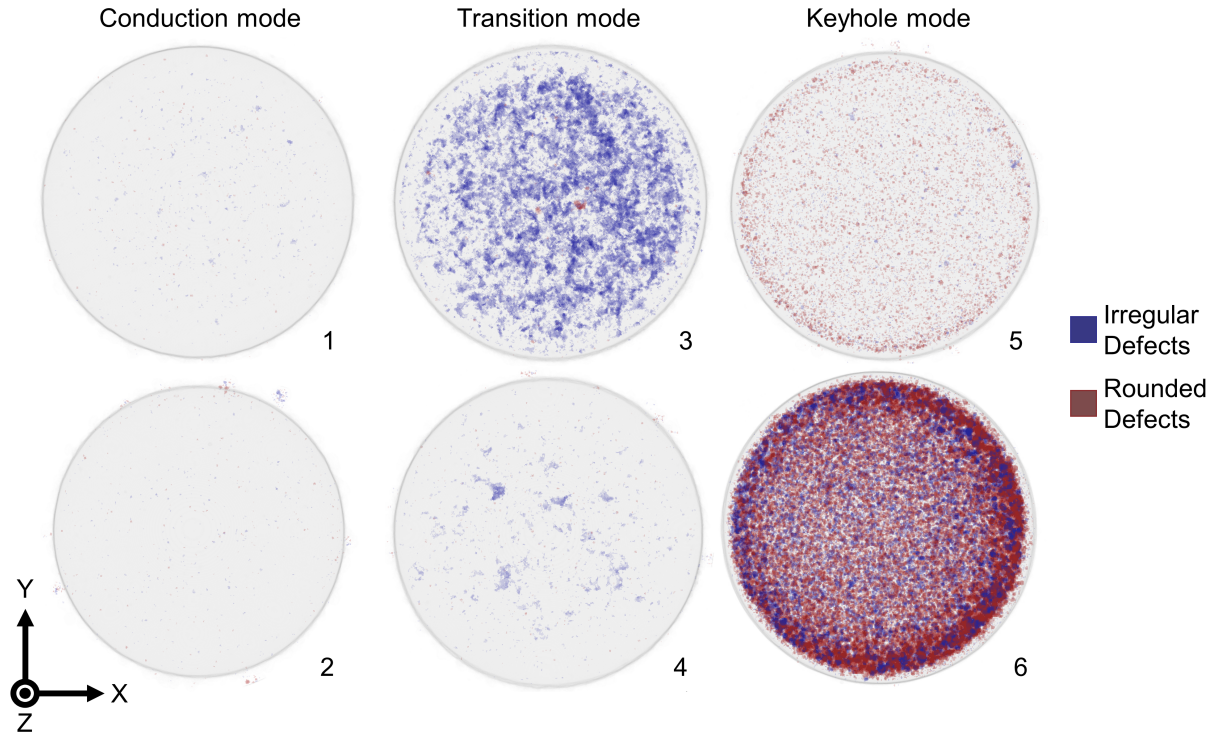


Figure 7: An orthographic projection of the porous defect (above 4 voxels) space along the build plate (XY) plane from the XCT data of the the conduction mode samples (1 and 2), transition mode samples (3 and 4), and keyhole mode samples (5 and 6). Defects with aspect ratios above 0.7 were considered as rounded defects.

could be associated to the inefficient laser expulsion of metal spatter as predicted by the analytical relationship derived by Khairallah et al. [32] in Equation 10 and visualized for the 21 focused beam processing parameters from Table 1 at a beam diameter of 70  $\mu\text{m}$  for the Renishaw AM 400 system in the left side of Figure 8.

Khairallah et al. [32] used a combination of high-fidelity simulations and high-speed X-ray imaging of LPBF to derive a criteria for stabilizing melt pool dynamics and minimizing defects. They derived an analytical relationship to help identify combinations of laser power and velocity that can help in preventing large metal spatter from blocking the center of a Gaussian laser beam. In Equation 10,  $H$  is the addition of the latent heat of fusion and vaporization, given by total latent heat in Table 2 and  $A_m$  the laser absorptivity of the melted surface of a given material which is assumed to the 0.15 (lowest conduction mode absorptivity in the present work and experimentally measured by Trapp et al. [30]). The term  $r_s$  in Equation 10 is the radius of a spatter particle under consideration.

$$P_{threshold} = \frac{\pi \rho r_s^3 (C_p (T_v - T_0) + H)}{3 A_m r_b} v \quad (10)$$

Khairallah et al. [32] observe that a spatter particle that is as large as the laser beam is capable of blocking the central high intensity region of a Gaussian laser beam, leading to sudden drop in melt pool depth. The rapid cooling caused by the sudden drop in melt pool depth thereby leads to defects as also observed by Martin et al. [74]. The radius of the spatter particle ( $r_s$ ) used to derive the spatter expulsion threshold through Equation 10 for Figure 8 is hence assumed to be the same as the beam radius (35  $\mu\text{m}$ ) used for the 21 samples codes that used a focused beam in Figure 8. The exact relationship used for Figure 8 is given by Equation 11.

$$P_{threshold} = 281 * v \quad (11)$$

Inefficient expulsion of spatter during LPBF of AlSi10Mg is confirmed to be a cause for lack of fusion defects in the transition and keyhole mode parameters (that use a focused beam) through representative micrographs on the right side of Figure 8. Sample codes 46, 50, and 57 (keyhole mode) are similar to sample code 3 (transition mode) in that they lie in the region wherein an inefficient laser expulsion of spatter is expected. This leads to a dominance of irregularly shaped lack of fusion defects, in line with the findings of Khairallah et al. [32]. A few rounded vaporization instability related defects are also observed in samples 46, 50, and 57 which would be expected due to the prediction of the keyhole melting mode for these samples in Figures 3 and 4. Sample 4 (transition mode) which shows very few lack of fusion defects lies very close to the spatter expulsion threshold. Sample codes 51, 52, and 53 (keyhole mode) have no lack of fusion defects in Figure 8. Samples 51, 52, and 53 are similar to sample 4 such that they all lie in the region wherein an efficient expulsion of spatter is expected as

per the left side of Figure 8. The primary source of defects in samples 51, 52, and 53 in the right side of Figure 8 is observed to be vaporization instability driven which is expected due to the prediction of the keyhole melting mode for these samples in Figures 3 and 4. Metal vaporization during LPBF was observed to be the largest driver of spatter issues by Khairallah et al. [32] and hence the divergent beam sample codes were not plotted in Figure 8 as they would not be affected by vaporization driven spatter related challenges, as predicted by Figure 3. For practical applications, the spatter expulsion threshold plotted in Figure 8 supplements the normalized processing diagram (Figure 3) and the keyhole number plot (Figures 4) by helping predict focused beam LPBF process parameter combinations that would help avoid deleterious lack of fusion defects by virtue of inefficient expulsion of laser spatter. The normalized processing diagram in Figure 3 helps in predicting the extent of vaporization for a given set of process parameters, and the keyhole number plot in Figure 4 helps in identifying the thresholds for the conduction, transition, and keyhole melting modes in LPBF.

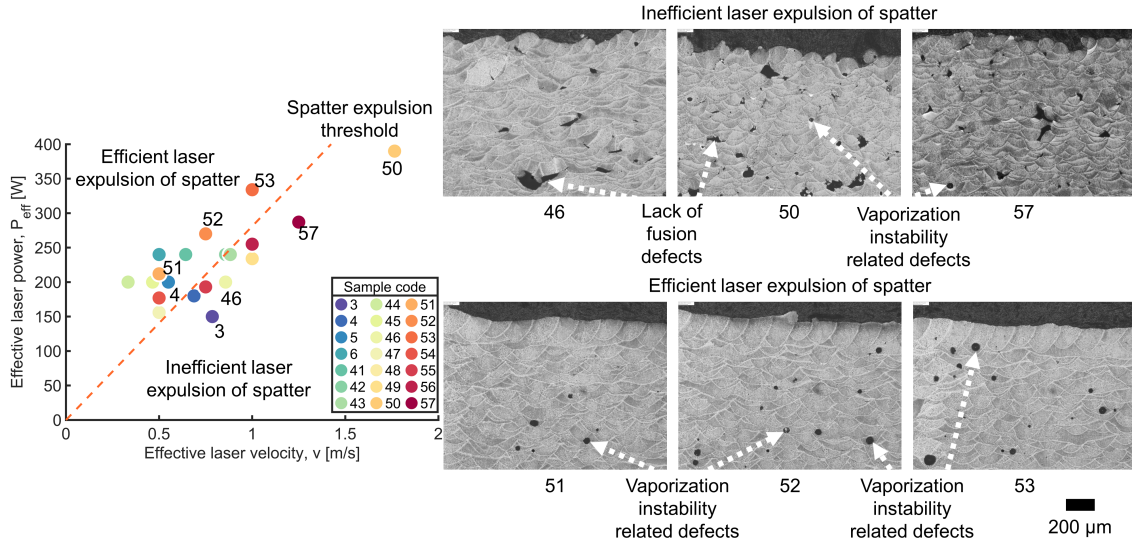


Figure 8: Spatter expulsion window based on effective laser power and velocity for LPBF of AlSi10Mg using a focused beam (beam radius = 35  $\mu\text{m}$ ) on the Renishaw AM 400 system (left). Micrographs of 3 sample codes (46, 50, and 57) that lie in the region of inefficient expulsion of spatter, and 3 samples codes (51, 52, and 53) that lie in the region of efficient expulsion of spatter (right).

There are additional reasons for the defects observed in the transition mode samples 3 and 4. Powder ejecta [75] and melt pool splatter caused by the breaking up of elongated molten pool regions near the side and rear walls of the vaporized region in transition and keyhole melting modes also contribute towards defect formation in samples 3 and 4 by adding to the roughness of a given layer [63]. Additionally, powder denudation [76, 77] also contribute towards the surface roughness of a given layer, thereby deteriorating the wetting behaviour of the following layers causing melt pool instabilities

and increasing the possibility of irregularly shaped defects as observed in the defect space visualization for samples 3, 4, 5, and 6 [78]. Although the average melt pool depth obtained for samples 3 and 4 (transition mode) is similar to sample 1 (conduction mode), the higher standard deviation in melt pool depths observed for samples 3 and 4 (Table 3) can lead to random regions where under-melting may occur if the melt pool is too shallow leading to irregularly shaped lack of fusion defects, or random regions where the process transitions into the keyhole melting mode leading to keyhole defects (sample 4 in Figure 5). The average melt pool widths of samples 3 and 4 are also lower when compared to samples 1 and 2, leading the possibility of lack of fusion defects caused by insufficient stitching of melt pools between hatches (hatch distance 100  $\mu\text{m}$ ) in a given layer. Additionally, as per Figure 3, it is predicted that surface vaporization has taken place in samples 3, 4, 5, and 6 leading to the possibility of defects related to the melt pool instabilities during transition melting mode in LPBF caused by the interplay between the drag force induced by the melt flow, the thermo-capillary force caused by the surface temperature gradients, and the recoil pressure introduced by the onset of material vaporization [63, 79, 74]. The defects obtained due to melt pool instabilities are known to have both rounded and irregularly-shaped morphologies [23, 80]. In a comparative study between the laser welding of an aluminium alloy and a ferrous alloy, the higher frequency of vaporized region collapse for aluminium alloys has been associated to the lower surface tension and viscosity of molten aluminium along with the presence of volatile magnesium which vaporizes at a temperature much lower than that of aluminium [81]. These observations are in line with the hypothesis proposed by Tenbrock et al. [35], wherein the importance of keyholes as a quasi-black body might be more pronounced for materials with higher reflectivity (e.g. aluminium and copper alloys) when compared to titanium, ferrous, and nickel alloys.

Samples 5 and 6 are predicted to lie in the keyhole melting mode by Figures 3 and 4. In the keyhole melting mode, vaporization related instabilities inside the melt pool would be expected to play a dominant role in the formation of rounded porous defects, as observed in Figures 6 and 7. To confirm this prediction, Figure 9 shows plots of aspect ratios of the defects versus frequency of defects and percentage of defect volume. The term frequency herein means the number of defects within a given sample identified by XCT. The aspect ratio data of the defects in Figure 9 and the volume data in Figure 10 is stored in 50 equally sized bins using MATLAB's built-in 'histcounts' function. A moving average of the frequency data with 5 nearest neighbours is then calculated using MATLAB's built-in 'movmean' which alongside the mid-point of each bin is used to interpolate the curves in Figure ?? and 10 by using MATLAB's built-in 'plot' function. Figure ?? was similarly obtained by creating a moving average of the volume data with respect to aspect ratio of the defects obtained from the XCT data.

The defect aspect ratio versus frequency plot in Figure ?? shows some indication to the preference of rounded defects in samples 5 and 6 (keyhole mode), but the aspect ratio versus percentage of defect volume plot provides a better understanding of such behaviour. Since the curves for samples 5 and 6

(keyhole mode) lean towards a higher aspect ratio in the plot against percentage of defect volume in Figure ??, it implies that most of the defects in samples 5 and 6 have a rounded morphology especially when compared to the other four samples. The rare occurrence of irregularly shaped defects can be associated to the higher average melt pool depths reported in Table 3, which are above two times the powder layer thickness used (30  $\mu\text{m}$ ). Typically, a melt pool depth of about 2 times (or more) the layer thickness is targeted in LPBF to avoid the possibility of lack of fusion defects [73].

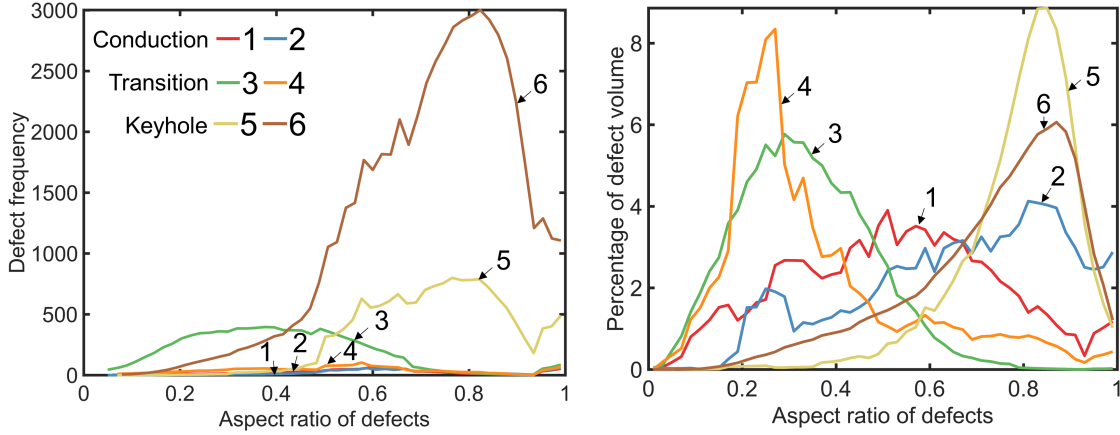


Figure 9: Aspect ratio of defects versus frequency of defects (a), and aspect ratio of defects versus percentage of defect volume (b) from the XCT data for sample codes 1-6 used for defect space evaluation in sections 3.2 and 3.3. Samples 1 and 2 are predicted to lie in the conduction melting, 3 and 4 in the transition melting mode, and 5 and 6 in the keyhole melting mode.

Figure 7 shows a higher concentration of rounded porous defects near the side walls of the cylinders for samples 5 and 6 (keyhole mode) that can be related to the rapid formation and collapse of deep vaporized regions due to the laser beam velocity at the turn points which occurs at the edges of a given layer in LPBF, thereby trapping the atmospheric gas in the solidified part [74]. A plot of defect volume versus frequency in Figure 10 reveals that most of the defects in samples 5 and 6 still belong to the lower volume regions of below  $0.0001 \text{ mm}^3$ . However, defects closer to the side wall of the cylinders would still be expected to impact its fatigue life, since the larger subsurface defects are the biggest factor impacting a parts fatigue life. The largest defect in sample 6 (keyhole mode) has a volume of  $0.0053 \text{ mm}^3$ . If this largest defect is assumed to be spherical, we would get a defect diameter of 0.22 mm which is close to the defects diameter of  $\sim 0.2 \text{ mm}$  that led to the fatigue crack initiation in AlSi10Mg as shown by Plessis et al. [46].

Samples 1 and 2 which are predicted to lie below the surface vaporization threshold (conduction melting mode) in Figures 3 and 4 seem to have almost no subsurface defects, with the sporadic occurrence of small defects typical to LPBF caused by random process factors or systematic machine biases [23]. Since no particular pattern is observed in the defect space for samples 1 and 2 from Figure 5,



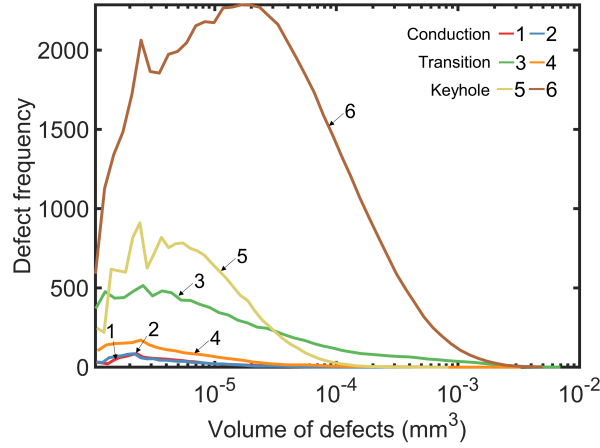


Figure 10: Volume of defects versus frequency of defects from the XCT data for sample codes 1-6 used for defect space evaluation in sections 3.2 and 3.3. Samples 1 and 2 are predicted to lie in the conduction melting, 3 and 4 in the transition melting mode, and 5 and 6 in the keyhole melting mode.

Figure 6, Figure 7, Figure 9, and Figure 10, the process parameter combinations involving the use of a divergent beam for samples 1 and 2 might be best suited for near fully dense LPBF AlSi10Mg components, particularly for systems with a smaller beam spot radius at the focal point.

Overall, when observing the melt pool morphology and porous defect characteristics across the melting modes in conduction (samples 1 and 2), transition (samples 3 and 4) and keyhole (samples 5 and 6), the benefit of deploying divergent beams in materials with a high reflectivity and high thermal conductivity becomes apparent. For these material systems, the use of a divergent beam as an energy source results in a more stable melt pool morphology, lower occurrence of porous defects in the core and sub-surface regions, and overall lower porous defect volumes. Furthermore, for such approaches, the hatch spacing, and power levels can be further optimized to minimize lack-of fusion random defects. For this class of material systems, while the use of a focused beam increases the challenge of finding stable melting process parameter combinations, the use of processing diagrams and dimensionless keyhole numbers as proposed in this work, alongside models for predicting the efficient expulsion of laser spatter can help identify stable melt pool morphologies, similar to the ones with divergent laser beams. It is important to note that the modelling and experimental approaches in this work would be particularly applicable to aluminium alloys that are not prone to cracking during LPBF such as AlSi10Mg, A357, Al-12Si, AlSi7Mg, Scalmalloy, etc [82]. Conventional high strength aluminium alloys from the 2000 (e.g. Al2024 [83]), 6000 (e.g. Al6061 [84, 85]), and 7000 (e.g. Al7075 [86]) series are geared towards manufacturing using forging techniques, and are prone to hot (solidification and liquation) cracking during LPBF; the behaviour of such alloys may not be fully predicted using the approaches highlighted in this present work. These alloys require approaches that can reduce the solidification stress

as well as the ratio of time spent by molten pool duration in the vulnerable zone (solid fraction between 0.9 and 0.99) to relaxation zone (solid fraction between 0.4 and 0.9) [87]. This has been accomplished previously in literature by either using compatible nanoparticle driven control of solidification [86], preheating the LPBF build plate [84], and/or using a high powered laser beam ( $\sim 1000$  W) [85].

#### 4. Conclusions

The influence of focused and divergent Gaussian laser beams on the melt pool dynamics, microstructure, and porous defects during the laser powder bed fusion of a high reflectivity aluminium alloy (AlSi10Mg) is investigated in this work. The key findings are summarized below:

1. Divergent beams help in avoiding keyhole defects by reducing the effective beam power density as the melt pool formation progresses, thereby leading to parts with densities of over 99.98%, with close to no porous defects in the subsurface regions, by conduction mode melting. Most defects observed in the conduction mode had volumes lower than  $0.00001 \text{ mm}^3$ . In contrast, keyhole mode melting led to relatively larger defects, with the largest defect having a volume of  $0.0053 \text{ mm}^3$ . This large keyhole mode defect with an equivalent diameter of 0.22 mm is similar in size to the defect that led to fatigue crack initiation in another study by Plessis et al. [46] on LPBF of AlSi10Mg.
2. Stabilizing melt pool and spatter dynamics in the transition melting mode by using an appropriate laser power and velocity combination can help in minimizing defects and obtaining densities close to 99.98%, similar to conduction mode densities.
3. A melt pool aspect ratio (ratio of depth to width) of  $\sim 0.4$  is observed to be the threshold between conduction and keyhole mode melt pools in AlSi10Mg, which differs from the conventionally assumed melt pool aspect ratio of 0.5.
4. The inferred absorptivity values for conduction mode melt pools (divergent beams) is  $0.24 \pm 0.05$ , while absorptivities of  $0.65 \pm 0.16$  are obtained for the transition and keyhole mode melt pools (focused beam), pointing to the significant differences in laser absorptivity following the onset of surface vaporization in aluminium alloys, when compared to titanium, nickel, and ferrous alloys, due to its higher reflectivity.
5. A higher standard deviation is observed in the melt pool depths for the transition mode (18% to 27%) and keyhole mode (4% to 35%) melt pools, when compared to the conduction mode (3% to 19%) melt pools. The predicted absence of vaporization in conduction mode melt pools is a likely cause for the relatively stable melting behaviour, when compared to transition and keyhole mode melt pools.



6. Conduction mode melting during LPBF of AlSi10Mg is expected within keyhole numbers (Ke) of 0-12, transition mode melting is expected within keyhole numbers of 12-20, and keyhole mode melting is expected for keyhole numbers greater than 20.

The application of the methods proposed in this work can help to quickly identify stable conduction mode LPBF processing parameters for high-reflectivity aluminium alloys. The presence of close to no defects even near the boundaries of LPBF components helps increase the confidence of the process for load bearing and mission critical applications in particular.

## Acknowledgements

Sagar Patel and Mihaela Vlasea appreciate the funding support received from Federal Economic Development Agency for Southern Ontario (FedDev Ontario grant number 081885). In addition, Sagar Patel and Mihaela Vlasea would like to acknowledge the help of Justin Memar for developing the CT analysis code; and the help of Lisa Brock, Hamed Asgari, Allan Rogalsky, Jerry Ratthapakdee, Grace Kurosad, and Henry Ma with the deployment and characterization of builds. Haoxiu Chen and Yu Zou acknowledge the financial support from Natural Sciences and Engineering Research Council of Canada (NSERC Discovery Grant number RGPIN-2018-05731). Haoxiu Chen also acknowledges the China Scholarship Council for a graduate fellowship (No.201906020162).

## References

- [1] J. Bonnín Roca, P. Vaishnav, E. R. H. Fuchs, M. G. Morgan, Policy needed for additive manufacturing, *Nature Materials* 15 (8) (2016) 815–818, number: 8 publisher: Nature Publishing Group. [doi:10.1038/nmat4658](https://doi.org/10.1038/nmat4658).
- [2] A. Gisario, M. Kazarian, F. Martina, M. Mehrpouya, Metal additive manufacturing in the commercial aviation industry: A review, *Journal of Manufacturing Systems* 53 (2019) 124–149. [doi:10.1016/j.jmsy.2019.08.005](https://doi.org/10.1016/j.jmsy.2019.08.005).
- [3] S. M. Wagner, R. O. Walton, Additive manufacturing’s impact and future in the aviation industry, *Production Planning & Control* 27 (13) (2016) 1124–1130. [doi:10.1080/09537287.2016.1199824](https://doi.org/10.1080/09537287.2016.1199824).
- [4] M. Gorelik, Additive manufacturing in the context of structural integrity, *International Journal of Fatigue* 94 (2017) 168–177. [doi:10.1016/j.ijfatigue.2016.07.005](https://doi.org/10.1016/j.ijfatigue.2016.07.005).
- [5] J. C. Najmon, S. Raesi, A. Tovar, 2 - review of additive manufacturing technologies and applications in the aerospace industry, in: F. Froes, R. Boyer (Eds.), *Additive Manufacturing for the Aerospace Industry*, Elsevier, 2019, pp. 7–31. [doi:10.1016/B978-0-12-814062-8.00002-9](https://doi.org/10.1016/B978-0-12-814062-8.00002-9).

- [6] S. Singamneni, L. Yifan, A. Hewitt, R. Chalk, W. Thomas, D. Jordison, Additive manufacturing for the aircraft industry: A review, *J. Aeronaut. Aerosp. Eng* 8 (1) (2019). doi:[10.1016/B978-0-12-814062-8.00002-9](https://doi.org/10.1016/B978-0-12-814062-8.00002-9).
- [7] T. DebRoy, T. Mukherjee, J. O. Milewski, J. W. Elmer, B. Ribic, J. J. Blecher, W. Zhang, Scientific, technological and economic issues in metal printing and their solutions, *Nature Materials* 18 (10) (2019) 1026–1032, number: 10 publisher: Nature Publishing Group. doi:[10.1038/s41563-019-0408-2](https://doi.org/10.1038/s41563-019-0408-2).
- [8] M. Delic, D. R. Eyers, J. Mikulic, Additive manufacturing: empirical evidence for supply chain integration and performance from the automotive industry, *Supply Chain Management: An International Journal* 24 (5) (2019) 604–621, publisher: Emerald Publishing Limited. doi:[10.1108/SCM-12-2017-0406](https://doi.org/10.1108/SCM-12-2017-0406).
- [9] M. Richardson, B. Haylock, Designer/maker: the rise of additive manufacturing, domestic-scale production and the possible implications for the automotive industry, *Computer-Aided Design & Applications PACE* 2 (2012) 33–48. doi:[10.3722/cadaps.2012.PACE.33-48](https://doi.org/10.3722/cadaps.2012.PACE.33-48).
- [10] K.-M. Hong, Y. C. Shin, Prospects of laser welding technology in the automotive industry: A review, *Journal of Materials Processing Technology* 245 (2017) 46–69. doi:[10.1016/j.jmatprotec.2017.02.008](https://doi.org/10.1016/j.jmatprotec.2017.02.008).
- [11] M. Delic, D. R. Eyers, The effect of additive manufacturing adoption on supply chain flexibility and performance: An empirical analysis from the automotive industry, *International Journal of Production Economics* 228 (2020) 107689. doi:[10.1016/j.ijpe.2020.107689](https://doi.org/10.1016/j.ijpe.2020.107689).
- [12] R. Leal, F. M. Barreiros, L. Alves, F. Romeiro, J. C. Vasco, M. Santos, C. Marto, Additive manufacturing tooling for the automotive industry, *The International Journal of Advanced Manufacturing Technology* 92 (5) (2017) 1671–1676. doi:[10.1007/s00170-017-0239-8](https://doi.org/10.1007/s00170-017-0239-8).
- [13] I. Gibson, D. Rosen, B. Stucker, M. Khorasani, Additive manufacturing technologies, Vol. 17, Springer, 2014. doi:[10.1007/978-3-030-56127-7](https://doi.org/10.1007/978-3-030-56127-7).
- [14] N. T. Aboulkhair, M. Simonelli, L. Parry, I. Ashcroft, C. Tuck, R. Hague, 3d printing of aluminium alloys: Additive manufacturing of aluminium alloys using selective laser melting, *Progress in Materials Science* 106 (2019) 100578. doi:[10.1016/j.pmatsci.2019.100578](https://doi.org/10.1016/j.pmatsci.2019.100578).
- [15] L. Brock, I. Ogunsanya, H. Asgari, S. Patel, M. Vlasea, Relative performance of additively manufactured and cast aluminum alloys, *Journal of Materials Engineering and Performance* 30 (1) (2021) 760–782. doi:[10.1007/s11665-020-05403-7](https://doi.org/10.1007/s11665-020-05403-7).

- [16] F. Trevisan, F. Calignano, M. Lorusso, J. Pakkanen, A. Aversa, E. P. Ambrosio, M. Lombardi, P. Fino, D. Manfredi, On the selective laser melting (slm) of the alsil0mg alloy: Process, microstructure, and mechanical properties, *Materials* 10 (1), pMID: 28772436 PMCID: PMC5344617 (1 2017). [doi:10.3390/ma10010076](https://doi.org/10.3390/ma10010076).
- [17] R. Cunningham, C. Zhao, N. Parab, C. Kantzos, J. Pauza, K. Fezzaa, T. Sun, A. D. Rollett, Keyhole threshold and morphology in laser melting revealed by ultrahigh-speed x-ray imaging, *Science* 363 (6429) (2019) 849–852, pMID: 30792298. [doi:10.1126/science.aav4687](https://doi.org/10.1126/science.aav4687).
- [18] M. Pastor, H. Zhao, R. Martukanitz, T. Debroy, Porosity, underfill and magnesium loss during continuous wave nd: Yag laser welding of thin plates of aluminum alloys 5182 and 5754, *Welding Journal* 78 (6) (1999) 207s–216s.
- [19] N. T. Aboulkhair, I. Maskery, C. Tuck, I. Ashcroft, N. M. Everitt, On the formation of alsil0mg single tracks and layers in selective laser melting: Microstructure and nano-mechanical properties, *Journal of Materials Processing Technology* 230 (2016) 88–98. [doi:10.1016/j.jmatprotec.2015.11.016](https://doi.org/10.1016/j.jmatprotec.2015.11.016).
- [20] L. Brock, Laser powder bed fusion of alsil0mg for fabrication of fluid power components, Master’s thesis, University of Waterloo (2020).
- [21] N. T. Aboulkhair, N. M. Everitt, I. Ashcroft, C. Tuck, Reducing porosity in alsil0mg parts processed by selective laser melting, *Additive Manufacturing* 1-4 (2014) 77–86. [doi:10.1016/j.addma.2014.08.001](https://doi.org/10.1016/j.addma.2014.08.001).
- [22] L. Thijs, K. Kempen, J.-P. Kruth, J. Van Humbeeck, Fine-structured aluminium products with controllable texture by selective laser melting of pre-alloyed alsil0mg powder, *Acta Materialia* 61 (5) (2013) 1809–1819. [doi:10.1016/j.actamat.2012.11.052](https://doi.org/10.1016/j.actamat.2012.11.052).
- [23] S. Patel, M. Vlasea, Melting modes in laser powder bed fusion, *Materialia* 9 (2020) 100591. [doi:10.1016/j.mtla.2020.100591](https://doi.org/10.1016/j.mtla.2020.100591).
- [24] H. Rao, S. Giet, K. Yang, X. Wu, C. H. Davies, The influence of processing parameters on aluminium alloy a357 manufactured by selective laser melting, *Materials & Design* 109 (2016) 334–346.
- [25] K. V. Yang, P. Rometsch, T. Jarvis, J. Rao, S. Cao, C. Davies, X. Wu, Porosity formation mechanisms and fatigue response in al-si-mg alloys made by selective laser melting, *Materials Science and Engineering: A* 712 (2018) 166–174.

- [26] A. B. Spierings, K. Dawson, M. Voegtlin, F. Palm, P. J. Uggowitzer, Microstructure and mechanical properties of as-processed scandium-modified aluminium using selective laser melting, *Cirp Annals* 65 (1) (2016) 213–216.
- [27] A. Mehta, L. Zhou, T. Huynh, S. Park, H. Hyer, S. Song, Y. Bai, D. D. Imholte, N. E. Woolstenhulme, D. M. Wachs, et al., Additive manufacturing and mechanical properties of the dense and crack free zr-modified aluminum alloy 6061 fabricated by the laser-powder bed fusion, *Additive Manufacturing* 41 (2021) 101966.
- [28] L. Zhou, H. Hyer, S. Park, H. Pan, Y. Bai, K. P. Rice, Y. Sohn, Microstructure and mechanical properties of zr-modified aluminum alloy 5083 manufactured by laser powder bed fusion, *Additive Manufacturing* 28 (2019) 485–496.
- [29] Z. Gan, O. L. Kafka, N. Parab, C. Zhao, L. Fang, O. Heinonen, T. Sun, W. K. Liu, Universal scaling laws of keyhole stability and porosity in 3d printing of metals, *Nature communications* 12 (1) (2021) 1–8.
- [30] J. Trapp, A. M. Rubenchik, G. Guss, M. J. Matthews, In situ absorptivity measurements of metallic powders during laser powder-bed fusion additive manufacturing, *Applied Materials Today* 9 (2017) 341–349. [doi:10.1016/j.apmt.2017.08.006](https://doi.org/10.1016/j.apmt.2017.08.006).
- [31] S. M. H. Hojjatzadeh, N. D. Parab, Q. Guo, M. Qu, L. Xiong, C. Zhao, L. I. Escano, K. Fezzaa, W. Everhart, T. Sun, L. Chen, Direct observation of pore formation mechanisms during lpbfd additive manufacturing process and high energy density laser welding, *International Journal of Machine Tools and Manufacture* 153 (2020) 103555. [doi:10.1016/j.ijmachtools.2020.103555](https://doi.org/10.1016/j.ijmachtools.2020.103555).
- [32] S. A. Khairallah, A. A. Martin, J. R. Lee, G. Guss, N. P. Calta, J. A. Hammons, M. H. Nielsen, K. Chaput, E. Schwalbach, M. N. Shah, et al., Controlling interdependent meso-nanosecond dynamics and defect generation in metal 3d printing, *Science* 368 (6491) (2020) 660–665.
- [33] J. Metelkova, Y. Kinds, K. Kempen, C. de Formanoir, A. Witvrouw, B. Van Hooreweder, On the influence of laser defocusing in selective laser melting of 316l, *Additive Manufacturing* 23 (2018) 161–169. [doi:10.1016/j.addma.2018.08.006](https://doi.org/10.1016/j.addma.2018.08.006).
- [34] T. Qi, H. Zhu, H. Zhang, J. Yin, L. Ke, X. Zeng, Selective laser melting of al7050 powder: Melting mode transition and comparison of the characteristics between the keyhole and conduction mode, *Materials & Design*[Online; accessed 2017-09-19] (2017). [doi:10.1016/j.matdes.2017.09.014](https://doi.org/10.1016/j.matdes.2017.09.014).
- [35] C. Tenbrock, F. G. Fischer, K. Wissenbach, J. H. Schleifenbaum, P. Wagenblast, W. Meiners, J. Wagner, Influence of keyhole and conduction mode melting for top-hat shaped beam profiles

- in laser powder bed fusion, *Journal of Materials Processing Technology* 278 (2020) 116514. doi:  
[10.1016/j.jmatprotec.2019.116514](https://doi.org/10.1016/j.jmatprotec.2019.116514).
- [36] M. Sow, T. De Terris, O. Castelnaud, Z. Hamouche, F. Coste, R. Fabbro, P. Peyre, Influence of beam diameter on laser powder bed fusion (l-pbf) process, *Additive Manufacturing* 36 (2020) 101532.
- [37] A. Aggarwal, S. Patel, A. Kumar, Selective laser melting of 316l stainless steel: Physics of melting mode transition and its influence on microstructural and mechanical behavior, *JOM*[Online; accessed 2019-02-13] (12 2018). doi:[10.1007/s11837-018-3271-8](https://doi.org/10.1007/s11837-018-3271-8).
- [38] J. Yang, J. Han, H. Yu, J. Yin, M. Gao, Z. Wang, X. Zeng, Role of molten pool mode on formability, microstructure and mechanical properties of selective laser melted ti-6al-4v alloy, *Materials & Design* 110 (Supplement C) (2016) 558–570. doi:[10.1016/j.matdes.2016.08.036](https://doi.org/10.1016/j.matdes.2016.08.036).
- [39] H. Wang, Y. Zou, Microscale interaction between laser and metal powder in powder-bed additive manufacturing: Conduction mode versus keyhole mode, *International Journal of Heat and Mass Transfer* 142 (2019) 118473. doi:[10.1016/j.ijheatmasstransfer.2019.118473](https://doi.org/10.1016/j.ijheatmasstransfer.2019.118473).
- [40] S. Patel, A. Rogalsky, M. Vlasea, Towards understanding side-skin surface characteristics in laser powder bed fusion, *Journal of Materials Research* 35 (15) (2020) 2055–2064. doi:[10.1557/jmr.2020.125](https://doi.org/10.1557/jmr.2020.125).
- [41] E. Brandl, U. Heckenberger, V. Holzinger, D. Buchbinder, Additive manufactured alsil0mg samples using selective laser melting (slm): Microstructure, high cycle fatigue, and fracture behavior, *Materials & Design* 34 (2012) 159–169. doi:[10.1016/j.matdes.2011.07.067](https://doi.org/10.1016/j.matdes.2011.07.067).
- [42] M. Tang, P. C. Pistorius, Oxides, porosity and fatigue performance of alsil0mg parts produced by selective laser melting, *International Journal of Fatigue* 94 (2017) 192–201. doi:[10.1016/j.ijfatigue.2016.06.002](https://doi.org/10.1016/j.ijfatigue.2016.06.002).
- [43] A. D. Brandão, J. Gumpinger, M. Gschweidl, C. Seyfert, P. Hofbauer, T. Ghidini, Fatigue properties of additively manufactured alsil0mg – surface treatment effect, *Procedia Structural Integrity* 7 (2017) 58–66. doi:[10.1016/j.prostr.2017.11.061](https://doi.org/10.1016/j.prostr.2017.11.061).
- [44] P. D. Enrique, A. Keshavarzkermani, R. Esmailizadeh, S. Peterkin, H. Jahed, E. Toyserkani, N. Y. Zhou, Enhancing fatigue life of additive manufactured parts with electrospray deposition post-processing, *Additive Manufacturing* 36 (2020) 101526. doi:[10.1016/j.addma.2020.101526](https://doi.org/10.1016/j.addma.2020.101526).
- [45] S. Leuders, M. Thöne, A. Riemer, T. Niendorf, T. Tröster, H. A. Richard, H. J. Maier, On the mechanical behaviour of titanium alloy ti6al4v manufactured by selective laser melting: Fatigue

- resistance and crack growth performance, *International Journal of Fatigue* 48 (2013) 300–307. [doi:10.1016/j.ijfatigue.2012.11.011](https://doi.org/10.1016/j.ijfatigue.2012.11.011).
- [46] A. du Plessis, I. Yadroitsava, I. Yadroitsev, Effects of defects on mechanical properties in metal additive manufacturing: A review focusing on x-ray tomography insights, *Materials & Design* 187 (2020) 108385. [doi:10.1016/j.matdes.2019.108385](https://doi.org/10.1016/j.matdes.2019.108385).
- [47] G. E. Bean, D. B. Witkin, T. D. McLouth, D. N. Patel, R. J. Zaldivar, Effect of laser focus shift on surface quality and density of inconel 718 parts produced via selective laser melting, *Additive Manufacturing* 22 (2018) 207–215, publisher: Elsevier.
- [48] T. Mukherjee, H. L. Wei, A. De, T. DebRoy, Heat and fluid flow in additive manufacturing – part ii: Powder bed fusion of stainless steel, and titanium, nickel and aluminum base alloys, *Computational Materials Science* 150 (2018) 369–380. [doi:10.1016/j.commatsci.2018.04.027](https://doi.org/10.1016/j.commatsci.2018.04.027).
- [49] J. C. Ion, H. R. Shercliff, M. F. Ashby, Diagrams for laser materials processing, *Acta Metallurgica et Materialia* 40 (7) (1992) 1539–1551.
- [50] Z. Chen, X. Wu, D. Tomus, C. H. J. Davies, Surface roughness of selective laser melted ti-6al-4v alloy components, *Additive Manufacturing* 21 (2018) 91–103. [doi:10.1016/j.addma.2018.02.009](https://doi.org/10.1016/j.addma.2018.02.009).
- [51] J. H. Robinson, I. R. T. Ashton, E. Jones, P. Fox, C. Sutcliffe, The effect of hatch angle rotation on parts manufactured using selective laser melting, *Rapid Prototyping Journal* 25 (2) (2019) 289–298, publisher: Emerald Publishing Limited. [doi:10.1108/RPJ-06-2017-0111](https://doi.org/10.1108/RPJ-06-2017-0111).
- [52] M. Dimter, R. Mayer, L. Hummeler, R. Salzberger, J. Kotila, T. Syvanen, [Method and device for manufacturing a three-dimensional object](#), source: Google Patents (10 2008). URL <https://patents.google.com/patent/US20080241392A1/en>
- [53] Z. W. Chen, T. Guraya, S. Singamneni, M. A. L. Phan, Grain growth during keyhole mode pulsed laser powder bed fusion of in738lc, *JOM* 72 (3) (2020) 1074–1084. [doi:10.1007/s11837-020-04012-y](https://doi.org/10.1007/s11837-020-04012-y).
- [54] C. Weingarten, D. Buchbinder, N. Pirch, W. Meiners, K. Wissenbach, R. Poprawe, Formation and reduction of hydrogen porosity during selective laser melting of als10mg, *Journal of Materials Processing Technology* 221 (2015) 112–120. [doi:10.1016/j.jmatprotec.2015.02.013](https://doi.org/10.1016/j.jmatprotec.2015.02.013).
- [55] S. P. Narra, Melt pool geometry and microstructure control across alloys in metal based additive manufacturing processes, Ph.D. thesis, Carnegie Mellon University (5 2017). [doi:10.1184/R1/6720569.v1](https://doi.org/10.1184/R1/6720569.v1).

- [56] L. R. Scime, Methods for the expansion of additive manufacturing process space and the development of in-situ process monitoring methodologies, Ph.D. thesis, Carnegie Mellon University, dOI: 10.1184/R1/6720581.v1 (5 2018).
- [57] X. Nie, Z. Chen, Y. Qi, H. Zhang, C. Zhang, Z. Xiao, H. Zhu, Effect of defocusing distance on laser powder bed fusion of high strength al-cu-mg-mn alloy, Virtual and Physical Prototyping 15 (3) (2020) 325–339. doi:10.1080/17452759.2020.1760895.
- [58] T. Graf, P. Berger, R. Weber, H. Hügel, A. Heider, P. Stritt, Analytical expressions for the threshold of deep-penetration laser welding, Laser Physics Letters 12 (5) (2015) 056002. doi:10.1088/1612-2011/12/5/056002.
- [59] Y. Huang, M. B. Khamesee, E. Toyserkani, A comprehensive analytical model for laser powder-fed additive manufacturing, Additive Manufacturing 12 (2016) 90–99. doi:10.1016/j.addma.2016.07.001.
- [60] Z. Zhang, Y. Huang, A. Rani Kasinathan, S. Imani Shahabad, U. Ali, Y. Mahmoodkhani, E. Toyserkani, 3-dimensional heat transfer modeling for laser powder-bed fusion additive manufacturing with volumetric heat sources based on varied thermal conductivity and absorptivity, Optics & Laser Technology 109 (2019) 297–312. doi:10.1016/j.optlastec.2018.08.012.
- [61] M. Matthews, J. Trapp, G. Guss, A. Rubenchik, Direct measurements of laser absorptivity during metal melt pool formation associated with powder bed fusion additive manufacturing processes, Journal of Laser Applications 30 (3) (2018) 032302. doi:10.2351/1.5040636.
- [62] J. Ye, S. A. Khairallah, A. M. Rubenchik, M. F. Crumb, G. Guss, J. Belak, M. J. Matthews, Energy coupling mechanisms and scaling behavior associated with laser powder bed fusion additive manufacturing, Advanced Engineering Materials 21 (7) (2019) 1900185.
- [63] S. A. Khairallah, A. T. Anderson, A. Rubenchik, W. E. King, Laser powder-bed fusion additive manufacturing: Physics of complex melt flow and formation mechanisms of pores, spatter, and denudation zones, Acta Materialia 108 (2016) 36–45. doi:10.1016/j.actamat.2016.02.014.
- [64] L. Gargalis, J. Ye, M. Strantza, A. Rubenchik, J. W. Murray, A. T. Clare, I. A. Ashcroft, R. Hague, M. J. Matthews, Determining processing behaviour of pure cu in laser powder bed fusion using direct micro-calorimetry, Journal of Materials Processing Technology 294 (2021) 117130.
- [65] W. Stopyra, K. Gruber, I. Smolina, T. Kurzynowski, B. Kuźnicka, Laser powder bed fusion of aa7075 alloy: Influence of process parameters on porosity and hot cracking, Additive Manufacturing 35 (2020) 101270.

- [66] W. E. King, H. D. Barth, V. M. Castillo, G. F. Gallegos, J. W. Gibbs, D. E. Hahn, C. Kamath, A. M. Rubenchik, Observation of keyhole-mode laser melting in laser powder-bed fusion additive manufacturing, *Journal of Materials Processing Technology* 214 (12) (2014) 2915–2925. doi:[10.1016/j.jmatprotec.2014.06.005](https://doi.org/10.1016/j.jmatprotec.2014.06.005).
- [67] S. D. Jadhav, L. R. Goossens, Y. Kinds, B. Van Hooreweder, K. Vanmeensel, Laser-based powder bed fusion additive manufacturing of pure copper, *Additive Manufacturing* 42 (2021) 101990.
- [68] Q. Chen, Y. Zhao, S. Strayer, Y. Zhao, K. Aoyagi, Y. Koizumi, A. Chiba, W. Xiong, A. C. To, Elucidating the effect of preheating temperature on melt pool morphology variation in inconel 718 laser powder bed fusion via simulation and experiment, *Additive Manufacturing* 37 (2021) 101642.
- [69] A. Kaplan, Metallurgy and imperfections of welding and hardening, in: *The Theory of Laser Materials Processing*, Springer, 2017, pp. 241–261. doi:[10.1007/978-3-319-56711-2\\_8](https://doi.org/10.1007/978-3-319-56711-2_8).
- [70] B. J. Simonds, J. Tanner, A. Artusio-Glimpse, P. A. Williams, N. Parab, C. Zhao, T. Sun, The causal relationship between melt pool geometry and energy absorption measured in real time during laser-based manufacturing, *Applied Materials Today* 23 (2021) 101049.
- [71] M. Salarian, H. Asgari, M. Vlasea, Pore space characteristics and corresponding effect on tensile properties of inconel 625 fabricated via laser powder bed fusion, *Materials Science and Engineering: A* 769 (2020) 138525. doi:[10.1016/j.msea.2019.138525](https://doi.org/10.1016/j.msea.2019.138525).
- [72] H. Asgari, M. Salarian, H. Ma, A. Olubamiji, M. Vlasea, On thermal expansion behavior of invar alloy fabricated by modulated laser powder bed fusion, *Materials & Design* 160 (2018) 895–905. doi:[10.1016/j.matdes.2018.10.025](https://doi.org/10.1016/j.matdes.2018.10.025).
- [73] Y. M. Wang, C. Kamath, T. Voisin, Z. Li, A processing diagram for high-density ti-6al-4v by selective laser melting, *Rapid Prototyping Journal* 24 (9) (2018) 1469–1478. doi:[10.1108/RPJ-11-2017-0228](https://doi.org/10.1108/RPJ-11-2017-0228).
- [74] A. A. Martin, N. P. Calta, S. A. Khairallah, J. Wang, P. J. Depond, A. Y. Fong, V. Thampy, G. M. Guss, A. M. Kiss, K. H. Stone, C. J. Tassone, J. N. Weker, M. F. Toney, v. T. Buuren, M. J. Matthews, Dynamics of pore formation during laser powder bed fusion additive manufacturing, *Nature Communications* 10 (1) (2019) 1987. doi:[10.1038/s41467-019-10009-2](https://doi.org/10.1038/s41467-019-10009-2).
- [75] A. R. Nassar, M. A. Gundermann, E. W. Reutzel, P. Guerrier, M. H. Krane, M. J. Weldon, Formation processes for large ejecta and interactions with melt pool formation in powder bed fusion additive manufacturing, *Scientific Reports* 9 (1) (2019) 5038. doi:[10.1038/s41598-019-41415-7](https://doi.org/10.1038/s41598-019-41415-7).



- [76] M. J. Matthews, G. Guss, S. A. Khairallah, A. M. Rubenchik, P. J. Depond, W. E. King, Denudation of metal powder layers in laser powder bed fusion processes, *Acta Materialia* 114 (2016) 33–42. [doi:10.1016/j.actamat.2016.05.017](https://doi.org/10.1016/j.actamat.2016.05.017).
- [77] P. Bidare, I. Bitharas, R. M. Ward, M. M. Attallah, A. J. Moore, Fluid and particle dynamics in laser powder bed fusion, *Acta Materialia* 142 (2018) 107–120. [doi:10.1016/j.actamat.2017.09.051](https://doi.org/10.1016/j.actamat.2017.09.051).
- [78] X. Zhou, D. Wang, X. Liu, D. Zhang, S. Qu, J. Ma, G. London, Z. Shen, W. Liu, 3d-imaging of selective laser melting defects in a co-cr-mo alloy by synchrotron radiation micro-ct, *Acta Materialia* 98 (2015) 1–16. [doi:10.1016/j.actamat.2015.07.014](https://doi.org/10.1016/j.actamat.2015.07.014).
- [79] S. M. H. Hojjatzadeh, N. D. Parab, W. Yan, Q. Guo, L. Xiong, C. Zhao, M. Qu, L. I. Escano, X. Xiao, K. Fezzaa, W. Everhart, T. Sun, L. Chen, Pore elimination mechanisms during 3d printing of metals, *Nature Communications* 10 (1) (2019) 1–8. [doi:10.1038/s41467-019-10973-9](https://doi.org/10.1038/s41467-019-10973-9).
- [80] S. Patel, M. Vlasea, Melting mode thresholds in laser powder bed fusion and their application towards process parameter development, in: *Proceedings of the 20th Annual International Solid Freeform Fabrication Symposium, Solid Freeform Fabrication Symposium, Austin, TX, 2019*, pp. 1190–1199.
- [81] L. Huang, X. Hua, D. Wu, F. Li, Numerical study of keyhole instability and porosity formation mechanism in laser welding of aluminum alloy and steel, *Journal of Materials Processing Technology* 252 (2018) 421–431. [doi:10.1016/j.jmatprotec.2017.10.011](https://doi.org/10.1016/j.jmatprotec.2017.10.011).
- [82] I. M. Kusoglu, B. Gökce, S. Barcikowski, Research trends in laser powder bed fusion of al alloys within the last decade, *Additive Manufacturing* 36 (2020) 101489.
- [83] G. Del Guercio, D. McCartney, N. Aboulkhair, S. Robertson, R. Maclachlan, C. Tuck, M. Simonelli, Cracking behaviour of high-strength aa2024 aluminium alloy produced by laser powder bed fusion, *Additive Manufacturing* (2022) 102776.
- [84] S. Z. Uddin, L. E. Murr, C. A. Terrazas, P. Morton, D. A. Roberson, R. B. Wicker, Processing and characterization of crack-free aluminum 6061 using high-temperature heating in laser powder bed fusion additive manufacturing, *Additive Manufacturing* 22 (2018) 405–415.
- [85] L. Loh, Z. Liu, D. Zhang, M. Mapar, S. Sing, C. Chua, W. Yeong, Selective laser melting of aluminium alloy using a uniform beam profile: The paper analyzes the results of laser scanning in selective laser melting using a uniform laser beam, *Virtual and Physical Prototyping* 9 (1) (2014) 11–16.

- [86] J. H. Martin, B. D. Yahata, J. M. Hundley, J. A. Mayer, T. A. Schaedler, T. M. Pollock, 3d printing of high-strength aluminium alloys, *Nature* 549 (7672) (2017) 365–369.
- [87] B. Mondal, T. Mukherjee, T. DebRoy, Crack free metal printing using physics informed machine learning, *Acta Materialia* 226 (2022) 117612.